Bioinspired 3D-printed scaffold embedding DDAB-nano ZnO/nanofibrous microspheres for regenerative diabetic wound healing

IOP Publishing Biofabrication 16 (2024) 015001 https://doi.org/10.1088/1758-5090/acfd60

Biofabrication

PAPER

Bioinspired 3D-printed scaffold embedding DDAB-nano ZnO/nanofibrous microspheres for regenerative diabetic wound healing

Walaa M Metwally[1], Salma E El-Habashy[1,*], Lobna S El-Hosseiny[2], Marwa M Essawy[3,4], Hoda M Eltaher[1,5,6,*] and Labiba K El-Khordagui[1,6]

[1] Department of Pharmaceutics, Faculty of Pharmacy, Alexandria University, Alexandria 21521, Egypt
[2] Department of Environmental Studies, Institute of Graduate Studies and Research, Alexandria University, Alexandria 21526, Egypt
[3] Oral Pathology Department, Faculty of Dentistry, Alexandria University, Alexandria 21500, Egypt
[4] Center of Excellence for Research in Regenerative Medicine and Applications (CERRMA), Faculty of Medicine, Alexandria University, Alexandria, Egypt
[5] Regenerative Medicine and Cellular Therapies Division, School of Pharmacy, Faculty of Science, University of Nottingham, Nottingham NG7 2RD, United Kingdom
[6] Last authors (equal contribution).
[*] Authors to whom any correspondence should be addressed.

E-mail: hoda.eltaher@nottingham.ac.uk, hoda.amin@alexpharmacy.edu.eg and salma.elhaleem@alexu.edu.eg

Keywords: hyaluronic acid-chitosan ink, polylactic acid, nanofibrous microspheres, bioinspired hydrogel scaffolds, customization, multilevel porosity, infected-wound healing

Supplementary material for this article is available online

OPEN ACCESS

RECEIVED
26 May 2023

REVISED
20 September 2023

ACCEPTED FOR PUBLICATION
26 September 2023

PUBLISHED
10 October 2023

Abstract

There is a constant demand for novel materials/biomedical devices to accelerate the healing of hard-to-heal wounds. Herein, an innovative 3D-printed bioinspired construct was developed as an antibacterial/regenerative scaffold for diabetic wound healing. Hyaluronic/chitosan (HA/CS) ink was used to fabricate a bilayer scaffold comprising a dense plain hydrogel layer topping an antibacterial/regenerative nanofibrous layer obtained by incorporating the hydrogel with polylactic acid nanofibrous microspheres (MS). These were embedded with nano ZnO (ZNP) or didecyldimethylammonium bromide (DDAB)-treated ZNP (D-ZNP) to generate the antibacterial/healing nano/micro hybrid biomaterials, Z-MS@scaffold and DZ-MS@scaffold. Plain and composite scaffolds incorporating blank MS (blank MS@scaffold) or MS-free ZNP@scaffold and D-ZNP@scaffold were used for comparison. 3D printed bilayer constructs with customizable porosity were obtained as verified by SEM. The DZ-MS@scaffold exhibited the largest total pore area as well as the highest water-uptake capacity and *in vitro* antibacterial activity. Treatment of *Staphylococcus aureus*-infected full thickness diabetic wounds in rats indicated superiority of DZ-MS@scaffold as evidenced by multiple assessments. The scaffold afforded 95% wound-closure, infection suppression, effective regulation of healing-associated biomarkers as well as regeneration of skin structure in 14 d. On the other hand, healing of non-diabetic acute wounds was effectively accelerated by the simpler less porous Z-MS@scaffold. Information is provided for the first-time on the 3D printing of nanofibrous scaffolds using non-electrospun injectable bioactive nano/micro particulate constructs, an innovative ZNP-functionalized 3D-printed formulation and the distinct bioactivity of D-ZNP as a powerful antibacterial/wound healing promotor. In addition, findings underscored the crucial role of nanofibrous-MS carrier in enhancing the physicochemical, antibacterial, and wound regenerative properties of DDAB-nano ZnO. In conclusion, innovative 3D-printed DZ-MS@scaffold merging the MS-boosted multiple functionalities of ZNP and DDAB, the structural characteristics of nanofibrous MS in addition to those of the 3D-printed bilayer scaffold, provide a versatile bioactive material platform for diabetic wound healing and other biomedical applications.

1. Introduction

The evolution of wound materials from conventional dressings to multifunctional wound protective/healing scaffolds is inevitably required for the advancement in the clinical management of infected chronic wounds including diabetic wounds and foot ulcers. Such wounds fail to progress through the normal healing phases because of the high-glucose environment leading to persistent bacterial infection, chronic inflammation, extensive oxidative stress as well as impaired angiogenesis, ECM function and immune response [1]. Therefore, advanced bioactive materials capable of providing the wound with mechanical protection and different combinations of wound microenvironment regulators are highly needed for effective diabetic wound healing [2].

Owing to their modifiable structural, physicochemical and drug release properties, hydrogels can effectively hasten the different phases of the healing process [3, 4]. The healing potential of hydrogels can be further augmented via the interplay of architectural, mechanical and biological engineering to obtain complex biomimetic regenerative constructs with multiple biological functionalities [5]. For instance, bioinspired bilayer scaffolds featuring the skin structure improve wound healing parameters including preservation of an anti-inflammatory microenvironment, suppression of oxidative stress, re-epithelialization, collagen organization, and neovascularization [6]. Modulating the hydrogel porosity is another structural approach contributing to improved diabetic wound healing [7].

Combining structural engineering with multiple biological functionalization using antimicrobial agents in addition to wound microenvironment regulators and regenerative biotherapeutics, e.g., growth factors, gene expression regulators, and cells, are rapidly evolving as multifunctional or 'all in one' strategies for effective acceleration of the healing process [8–10]. In this context, antimicrobial agents play a crucial role in clearing up infection at the wound site, reducing the risk of necrosis and lower limb amputation. Apart from antibiotics [11, 12], newer agents such as antimicrobial peptides and peptide-based polymers [13], phytochemicals [14, 15] and inorganic nanomaterials such as silver nanoclusters [16], Au-based nanoparticles (NPs) [17], and metal oxide NPs, e.g. zinc oxide [15], magnesium oxide, cerium oxide and ferric oxide NPs [18] are currently emerging as effective bioactives capable of preventing infection, reducing bacterial resistance and promoting healing of acute and diabetic wounds. Different composites made of polymeric biomaterials and antimicrobial metal-based nanostructures, such as Ag NPs and ZNP as substitutes for antibiotics, inhibit bacterial growth with simultaneous acceleration of the healing process [19]. A recent review highlighted the antimicrobial activity of ZNP biocomposites fabricated as films, hydrogels, or electrospun scaffolds for wound healing applications including diabetic wounds [20]. Clinically, composite ZNP/calcium alginate dressings were shown to improve tissue regeneration in diabetic patients while avoiding complications of type 2 diabetes [21]. The antibacterial mechanism of ZNP potentially involves electrostatic interaction with bacterial cell membrane, release of Zn^{2+} ions and generation of reactive oxygen species [22]. In addition, ZNP exert an antioxidant/anti-inflammatory effect and enhance the migration of keratinocytes and epithelial cells, speeding wound repair [23].

The integration of multiple bioactives in a single biomaterial platform featuring complex geometries and functionalities is a real biomedical engineering challenge that could be successfully met by 3D printing technology. The technique allows computer-based production of multilayer 3D constructs with versatile structural and biological attributes [24]. The commonly used extrusion-based 3D printing modality depends on inks often made of bioactive polysaccharide polymers such as hyaluronic acid (HA), sodium alginate and chitosan (CS) as well as peptides and proteins [25–27]. As a nanofibrous (NF) component would endow the 3D printed scaffold with physical nanopores alongside the space available between adjacent cross-links in the hydrogel polymer network, inclusion of electrospun NF may promote cell anchoring and regenerative healing. Composite hydrogel/NF architectures can be achieved by combining 3D printing and electrospinning technologies [28]. Reported designs involved NF interleaves between printed layers [29], composite core/shell fiber scaffolds [30, 31] or hydrogels incorporating short NFs [32].

As the need for improvement is continual, we propose herein an innovative multifunctional bilayer 3D printed scaffold based on a blend of the polysaccharide polymers: HA and CS as 3D printing ink, for regenerative treatment of diabetic wounds taking into consideration simple composition and easy fabrication. A HA/CS blend would synergistically enhance wound healing owing to the anti-inflammatory, antioxidant and cell function-promoting effects of HA combined with the antibacterial activity and bioadhesive properties of CS [33]. Both the architecture and bioactivation of the adopted scaffold differ from previously reported antimicrobial hydrogels. The scaffold presented an innovative bioinspired bilayer hydrogel structure, with a

relatively dense plain HA/CS epidermis-mimicking protective layer topping a more porous bioactive antimicrobial/regenerative dermis-mimicking layer of the same hydrogel. The bottom layer was bioactivated utilizing the injectable NF inorganic/organic hybrid microconstructs recently developed by our team [22]. The microconstructs comprise NF PLA microspheres (MS) incorporating zinc oxide NPs (ZNP) or DDAB-treated ZNP (D-ZNP) as single multifunctional bioactive MS (ZNP@MS or D-ZNP@MS). The microconstructs are highly stable spherical micromeshes having a mean diameter of $\sim$ 24.5 μm and mean NF diameter of $\sim$ 104 nm. They exhibit marked *in vitro* antibacterial activity against *Staphylococcus aureus* (*S. aureus*), hemostatic effects both *in vitro* and *in vivo* and controllable concentration-dependent cytotoxicity on human gingival fibroblasts. The antibacterial effect of ZNP was significantly augmented by DDAB treatment, corroborating literature data [34]. Besides, both ZNP@MS and D-ZNP@MS micromeshes promoted cell migration in the scratch assay, offering potential as multifunctional wound biomaterials. On the other hand, the MS carrier matrix provided a large surface area for uniform dispersion of nanomaterials, thereby reducing agglomeration and enhancing cellular interactions. The micromeshes enhanced the release of Zn^{2+} ions from ZNP and D-ZNP in a sustained manner and enhanced their cytotoxic and hemostatic effects.

As such, the objective of the study was to fabricate an innovative NF regenerative diabetic wound healing biomaterial using 3D printing as the sole technique and ZNP or D-ZNP embedded into NF MS as single multifunctional bioactive agents. Moreover, the MS meshes would impart nanoporosity to the microporous HA/CS hydrogel, generating multilevel porosity to stimulate cell spreading and adhesion, of importance to tissue in-growth [35]. Additionally, sustained release of Zn^{2+} by MS would promote a lasting antibacterial effect at the wound site. This is the first study documenting the utilization of NF ink for the 3D printing of NF hydrogel scaffolds. Secondly, although different ZNP-based film, hydrogel, electrospun formulations have been reported [19, 20], the wound healing efficacy of ZNP-bioactivated 3D printed scaffolds has not been documented to date. Thirdly, the *in vivo* wound healing performance of D-ZNP has not been evaluated despite remarkable *in vitro* antibacterial activity [34] and highly promising *in vitro* wound healing aptitudes and hemostatic potential [22]. Formulation and characterization of plain and composite HA/CS-based inks were performed for the fabrication of bioinspired bilayer scaffolds with customizable chemical composition and porosity. Afterwards, the wound healing efficacy of the DZ-MS@scaffold in comparison with Z-MS@scaffold and their respective component scaffolds was assessed at the macroscopical, microscopical and molecular levels utilizing an experimental infected diabetic wound healing model in rats. In addition, the efficacy of the simpler Z-MS@scaffold in accelerating the healing of infected diabetic and non-diabetic wounds was assessed to demonstrate the opportune tunability of the 3D printing technique to satisfy different wound healing demands.

2. Materials and methods

2.1. Materials

Poly (lactic acid) (PLA, Mw = 280 kDa, Mw/Mn = 1.98) was purchased from Natureworks (LLC, USA). Sodium hyaluronate (HA, Mwt 1000–1500 kDa) was obtained from Lotioncrafter (LLC, WA, USA). Chitosan (CS, medium Mwt: 100–300 kDa; degree of deacetylation >85%) was obtained from Acros Organics™ (New Jersey, USA). Zinc acetate dihydrate (Zn $(CH_3COO)_2 \cdot 2H_2O$; 98% purity) was purchased from Loba Chemie (Mumbai, India). Didecyldimethylammonium bromide (DDAB) was purchased from Chem Impex (Blair, NE, USA). Streptozotocin (SPZ, >97%) was purchased from MP Biomedicals, USA. Glacial acetic acid, glycerol, hydrochloric acid (HCl), sodium hydroxide (NaOH) and tetrahydrofuran (THF) were purchased from Adwic, El-Nasr Pharmaceutical Co (Cairo, Egypt). Müeller Hinton broth and Müeller Hinton agar were obtained from Oxoid (UK). Other reagents used in the experiment were of analytical grade and no further purification was required.

2.2. Development and characterization of blank and NF 3D printable inks

2.2.1. Preparation of composite NF MS

Blank PLA NF MS were produced using a thermally induced phase separation technique [22]. In brief, a PLA solution (2% w/v) in THF was homogenized with glycerol in an organic: aqueous phase ratio of 1:3 at 6000 rpm for 5 min at 50 °C. The mixture was then quenched in liquid nitrogen and solvent exchange was allowed using ice-cold deionized water at 4 °C for 24 h. NF MS bioactivated with ZNP (Z-MS) or D-ZNP (DZ-MS) were synthesized via uniform dispersion of ZNP or D-ZNP (1.5% DDAB) in the PLA solution (2% w/v) in THF at 50 °C to achieve a final NP concentration of 50% w/v prior to MS formation.

2.2.2. Ink preparation

Inks were prepared using a HA/CS polymer blend. The aqueous solution of HA (5% w/v) was prepared in deionized water, then CS was homogenously

dispersed by simple mixing at different final concentrations (5%, 12.5%, and 25% w/v), achieving HA/CS weight ratios of 1:1, 1:2.5, 1:5, respectively.

For the preparation of composite NF inks (Z-MS@ink and DZ-MS@ink), Z-MS or DZ-MS containing the equivalent of 1.25% of the NP were uniformly dispersed by mixing with the plain ink containing 12.5% CS. Control inks containing blank NF MS (blank MS@ink) or 1.25% NP (ZNP@ink and D-ZNP@ink) were prepared for comparison.

2.2.3. Ink characterization

2.2.3.1. Spreading ratio

The spreading ratio of the developed inks was determined by normalizing the printed filament diameter of each ink to the needle diameter [36]. Each filament was printed five times under the same conditions, images were captured, and the filament diameter was measured using image analysis software (Fiji version 1.52p; National Institutes of Health, Maryland, USA). Spreading ratio was calculated using equation (1) [37]:

$$\text{Spreading ratio} = \frac{\text{Printed filament diameter}}{\text{Nozzle diameter}}. \quad (1)$$

2.2.3.2. Viscosity measurements

The viscosity of the test inks was measured using a digital viscometer (DV2T viscometer, Brookfield, Massachusetts, USA) over a shear rate range of 0.037–0.110 s^{-1} at 25 °C.

2.2.4. In vitro *assessment of the antibacterial activity of test inks*

The antibacterial activity of the test inks against *S. aureus* ATCC 29 213 was determined using the broth microdilution method [38]. An overnight culture of *S. aureus* in Müeller Hinton broth was adjusted to 0.5 Mcfarland turbidity standard. Two-fold serial dilutions of the test inks ranging from 625 to 4.88 $\mu g\ ml^{-1}$ of ZNP and D-ZNP were added to the bacterial suspension in a 96 well microtiter plate. Inoculated Müeller Hinton broth was used as growth control whereas uninoculated Müeller Hinton broth served as sterility control. The microtiter plate was incubated at 37 °C for 24 h and the lowest concentration of the test ink which inhibited visible growth following incubation was assigned as the respective MIC.

2.2.5. Assessment of S. aureus morphological features

The effect of DZ-MS@ink on *S. aureus* morphology was assessed by scanning electron microscopy (SEM). Overnight *S. aureus* culture adjusted to 0.5 Mcfarland turbidity standard was treated with one MIC of DZ-MS@ink. Both control untreated and treated cultures were incubated at 37 °C for 4 h and centrifuged at 4000 × g for 10 min. The centrifuged bacterial cells were washed thrice with 0.1 M phosphate buffer saline (PBS, pH 7.4) and fixed with 2.5% glutaraldehyde. Samples were sequentially dehydrated with graded ethanol concentrations (50%–100% w/v) for 10 min each, sputter coated with gold and examined using SEM (JSM-IT200; JEOL, Tokyo, Japan).

2.3. Design and characterization of 3D printable bilayer/bioinspired scaffolds

The design of the 3D scaffold structure was constructed using a 3D CAD tool (Tinkercad®; Autodesk, California, USA). Scaffolds were designed as bilayer cylindrical/disc structures having the dimensions: 15 mm diameter and 2.5 mm height (0.5 mm top- and 2 mm bottom-layer). The extrusion-based 3D printing process was conducted using a 0.5 mm nozzle diameter at 3 mm s^{-1} printing speed and 100% or 75% ink flow level. The percentage flow level is an indicator of the amount of extruded ink during printing [39], where a 75% ink flow implies a 25%-reduction in the amount of deposited ink and hence an increase in structure porosity. Printing was performed at ambient temperature (∼25 °C) in a layer-by-layer deposition manner using a 3D printer (Robota, Alexandria, Egypt) equipped with dual extruders enabling a dual printing process. Crosslinking was achieved via *in situ* layered spraying of acetic acid solution of different concentrations (2, 4, 6 and 8% v/v) [40], (2.35 ± 0.13 μl per layer). The printed scaffolds were washed three times with deionized water to remove excess crosslinker and thereby freeze-dried (Lyoquest; Telstar, Terrassa, Spain).

2.3.1. SEM

The microstructure, pore size and total pore area of the test 3D-printed scaffolds were examined by SEM. Before examination, freeze-dried scaffolds were vertically sectioned, placed on a conductive adhesive tape on metal stubs and coated with gold using a sputter coater. SEM images were captured, then measurements were performed from at least 50 micrographs using the image analysis software.

2.3.2. Mechanical properties

The mechanical properties of the 3D-printed scaffolds were examined using a texture analyzer (CT3; Brookfield, Massachusetts, USA). Freeze-dried scaffolds were first wetted with saline for mimicking the *in vivo* setting and compressed at a 75% strain and 1 mm s^{-1} compression speed. The ultimate compressive strength was recorded, and the stress–strain curve established. The elastic modulus (Young's modulus) was calculated as the slope of the linear part of the stress–strain curve.

2.3.3. Swelling behavior

The swelling behavior of the 3D-printed scaffolds was assessed by determining the percentage water uptake

over 14 d. After recording their dry weights (W_0), scaffolds were allowed to swell in 5 mL deionized water at 37 °C with shaking at 50 rpm (Wisebath shaking water bath; Daihan Scientific Co. Ltd, Seoul, South Korea). At predetermined time points, the wet scaffolds were removed, gently blotted against filter paper and re-weighed (W_t). The percentage swelling was calculated according to equation (2) [41]:

$$Swelling\ (\%) = \frac{W_t - W_0}{W_0} \times 100 \qquad (2)$$

W_0 and W_t represent the weight of dry scaffold at time zero and weight of wet scaffold at time t, respectively.

2.3.4. Fourier transform infrared spectroscopy (FTIR)
Samples were analyzed using FTIR (Agilent Cary 630; Agilent technologies, CA, USA). Spectra were obtained in the wave number range of 4000–650 cm^{-1} with a resolution of 2 cm^{-1}.

2.3.5. X-ray diffraction (XRD) analysis
XRD patterns were obtained using x-ray diffractometer (Bruker D2-Phaser; Madison, WI, USA) at room temperature. The operating parameters were 30 kV and 10 mA with Cu Kα monochromatic radiation at a wavelength of 1.54184 Å. Measurements were performed with diffraction angle (2θ) scanned in the range of 10° to 80°, at a step size of 0.01° and a step time of 0.05 s.

2.4. Wound healing studies in a rat model
The wound healing efficacy of the composite 3D printed scaffolds was assessed using infected full-thickness excision diabetic wounds in rats, recapitulating features of a chronic wound model [42]. A non-diabetic acute wound model was also adopted for comparison. G* Power, version 3.1.9.7, was used to estimate the appropriate sample size employing replacement, reduction, and refinement principles for the responsible use of animals in bioscience research. Using a priori calculation, sample size was calculated from literature studies involving diabetic wound healing represented as percentage wound closure at day 14 [43–46], based on 95% confidence intervals and 80% power criteria as shown in table S1.

All animal procedures were performed after obtaining approval of the Institutional Animal Care and Use Committee (IACUC), Alexandria University, Egypt (AU 0620191214165). Experiments complied with the ARRIVE guidelines and were carried out in accordance with the U.K. Animals (Scientific Procedures) Act, 1986 and associated guidelines, EU Directive 2010/63/EU for animal experiments. Thirty-two healthy male Wistar rats weighing 225 ± 25 g, provided by the animal facility of the Faculty of Medicine, Alexandria University, Egypt, were housed at room temperature and provided with water and food ad libitum for 2 adaptation weeks. Rats were randomly divided into two major groups, group A for infected diabetic (chronic) wounds and group B for non-diabetic (acute) wounds.

2.4.1. Infected diabetic/chronic wound model-group A
2.4.1.1. Induction of diabetes mellitus
Twenty-four rats were fasted for 24 h before induction of diabetes mellitus via intraperitoneal injection of a single streptozotocin dose (45 mg kg^{-1}) dissolved in 0.1 M citrate buffer (pH 4.5). Rats were immediately administered oral sucrose solution to reduce streptozotocin-induced hypoglycemia. Three days later, blood glucose level was measured using a digital glucometer (ONETOUCH® Select™; LifeScan, Wayne, PA) and rats with glucose level above 250 mg dl^{-1} were considered diabetic [42]. Blood glucose level of diabetic rats was repeatedly measured throughout the study period to ensure the diabetic state.

2.4.1.2. Establishment of full-thickness excision wounds
Full-thickness excision wounds were made three days after induction of diabetes. Anesthesia was induced via intraperitoneal injection of ketamine hydrochloride (75 mg kg^{-1}) and xylazine (10 mg kg^{-1}). The hair of all the mid-dorsal skin was then shaved, and the shaved area was disinfected with topical Betadine® solution. Two full-thickness excision wounds (1.5 cm diameter) were surgically created on both sides of the dorsal region of each rat to the depth of loose subcutaneous tissue, using a sterile biopsy punch and surgical scissors. The wound area was thoroughly cleansed with sterile normal saline (0.9% w/v NaCl). Infection was then established by inoculating a suspension of 1×10^8 CFU/ml *S. aureus* ATCC 29 213 into the wounds. Guided by power analysis using different studies [43–46], an overall sample size of 16 was determined to be the minimum number of rats required ($n = 2$ per group). Sample size was increased to 4 per group to account for potential attrition and to perform proper statistical analyses. Afterwards, rats were randomly divided into six subgroups ($n = 4$); where wounds were untreated (diabetic control) or treated with sterile plain scaffolds or scaffolds loaded with D-ZNP, blank MS, Z-MS or DZ-MS (corresponding to 1% w/w NP final concentration). Wounds were further dressed by suturing a polyurethane film (Tegaderm™, 3 M, USA) over the wound bed [12], and padded with sterile gauze and surgical tape. Finally, rats were separated into individual cages with unrestricted access to food and water. Wound dressing was replaced every other day. Animals were sacrificed on day 14 post-surgery with an overdose of isoflurane, and full thickness wound tissue autopsies were collected.

2.4.2. Non-diabetic/acute wound model-group B

Eight non-diabetic rats were employed for the development of the acute non-diabetic wound model. Full-thickness excision wounds were created as described for diabetic wounds, however, wounds were not inoculated with bacteria prior to treatment. The acute wound healing accelerating effect of Z-MS@scaffold was assessed, in comparison to untreated, non-diabetic control wounds ($n = 4$). Animals were sacrificed 14 d after surgery and full thickness tissue autopsies of regenerated tissues were obtained.

2.4.3. Wound healing assessment

2.4.3.1. Evaluation of wound closure

The wound site for rats in both groups A and B was photographed immediately after surgery (day 0) and at specific time intervals post-surgery (days 3, 7 and 14), to assess the reduction of wound size. The wound area was analyzed using image analysis software. The percentage wound closure was calculated using equation (3) [12]:

$$\text{Percentage wound closure } (\%) = \frac{\text{Wound area on day 0} - \text{Wound area on day t}}{\text{wound area on day 0}} \times 100. \quad (3)$$

2.4.3.2. Microbiological examination of infected diabetic wound

The bacterial burden of the microbiologically challenged diabetic wounds was assessed on days 7 and 14 post wounding. The bacterial count for untreated diabetic control at each time interval after wound inoculation was assigned as 100% of the expected bacterial count for each group. Wound swabs were mixed with 1 ml sterile normal saline and vortexed thoroughly. Thereafter, ten-fold serial dilutions were prepared and plated onto Müeller Hinton agar for determination of bacterial counts after incubation at 37 °C for 24 h. The number of colonies was counted using an auto-colony counter, expressed as CFU/mL and normalized to untreated control for determination of percentage bacterial count reduction ($n = 3$).

2.4.3.3. Histological examination and histomorphometric analysis

For histological examination, the wound tissue extracted 14 d after surgery (wound bed with 1 cm around the margin and 1 cm depth) was fixed in 10% neutral buffered formalin for 48 h. Specimens were gradient-dehydrated and embedded in paraffin with their epidermal-dermal surface oriented toward the cutting plane to obtain 4–5 μm serial sections from three planes: wound center and 50–75 μm on either side of the center. Subsequently, slide sections were stained with hematoxylin & eosin (H&E) and Masson's Trichrome stains. For gross histological examination of the wound area (mainly from the centered cut plane), digital images were captured at $\times 40$ and $\times 100$ magnifications, including the epidermal and dermal layers using a digital camera (Olympus DP20, Japan) connected to the microscope (Olympus BX41, Japan). For a detailed qualitative and morphometric evaluation of the wounds, high-powered digital images were further taken at $\times 200$ and $\times 400$ magnifications.

The inflammatory score, interpreted double-blindly from the H&E-stained sections, was as follows: score 1 for sparse, score 2 for focal, score 3 for multifocal coalescent and score 4 for diffuse-inflammatory infiltrates [40]. The reciprocal intensity of fibrosis from the $\times 400$ captured trichrome-stained photomicrographs was calculated using equation (4):

$$RI = 255 - \textit{mean intensity}, \quad \text{where 255 is the maximum intensity.} \quad (4)$$

2.4.3.4. Quantification of healing-associated biomarkers

Quantitative reverse transcription polymerase chain reaction (RT-qPCR) was employed to investigate the expression level of tumor necrosis factor-alpha (TNF-α). Tissue autopsies were homogenized in bioZOL reagent for RNA extraction, and RNA quantification was conducted (NanoDrop DS-11 FX; DeNovix, USA). cDNA was synthesized using a RevertAid First Strand cDNA Synthesis Kit (Thermofisher) using random primers according to manufacturer's instructions. RT-qPCR was performed using SYBR Green Supermix and run on a CFX96 Real-Time Thermal Cycler (Bio-Rad, USA). Primer sequence for TNFα was: (forward): 5′-GGTGCCTATGTCTCAGCCTC-3′; (reverse): 5′-GCTCCTCCACTTGGTGGTTT-3′ and for glyceraldehyde-3-phosphate dehydrogenase (GAPDH): (forward): 5′-TGCCCCCATGTTTGT GATG-3′; (reverse): 5′-TGTGGTCATGAGCCCTTCC-3′ (Eurofins Scientific, Luxembourg). Expression of TNF-α was quantified by normalization to the house keeping GAPDH gene, adopting the $2^{-\Delta\Delta Ct}$ method.

The levels of vascular endothelial growth factor (VEGF) and epidermal growth factor (EGF) expressed in the regenerated wound tissue were quantified using Enzyme-Linked Immunosorbent Assay (ELISA). The collected tissue samples were homogenized in an ice-bath, then tissue homogenate was centrifuged at 5000 $\times$ g for 5 min at 4 °C, and the supernatant was collected for ELISA. Quantitative analysis was conducted using rat VEGF or EGF ELISA kits (CUSABIO, Wuhan, China) in accordance with the manufacturer's instructions. Concentrations were normalized to protein content and were expressed as pg/mg protein.

2.5. Statistical analysis

Experiments were run at least in triplicate and data were presented as the mean $\pm$ standard deviation

(SD). Results were analyzed by conducting Student's t-test or analysis of variance (ANOVA) followed by Tukey's post-hoc comparison tests using SPSS® software (SPSS Inc., Chicago, IL, USA). Unless otherwise mentioned, values of $p < 0.05$ were considered statistically significant.

3. Results and discussion

3.1. Development of plain and NF HA/CS 3D-printable inks

Biocompatibility, bioactivity, mechanical properties, extrusion efficiency, and high post-printing shape fidelity are pivotal requirements for developing 3D printing inks intended for biomedical applications. The ink printing performance may be considerably affected by the inclusion of particulate elements (NP or MS) [40]. Herein, innovative NF inks were developed for the fabrication of a multifunctional scaffold for regenerative wound healing. The ink consists of a blend of HA/CS polymers composited with PLA NF MS embedding ZNP and D-ZNP as antibacterial nanomaterials.

Despite the favorable biological properties of HA as 3D printing hydrogel precursor [47], its poor mechanical strength and fast degradation rate under physiological conditions limit its 3D printing applications. HA printability and biostability can be improved by chemical modification and/or mixing with other polymers exhibiting better printing properties [41]. In this context, CS offers unique merits as printing ink element including appropriate viscosity, adequate mechanical properties, and stability under physiological conditions [48]. In addition, inclusion of CS in various ink compositions would endow the printed scaffolds with antibacterial activity. HA/CS hydrogels either based on polyelectrolyte complexation or simple mixing were reported to exhibit cytocompatibility and promising printing properties [37, 49]. Thus, HA/CS inks were investigated for the development of inks with different compositions.

3.1.1. HA/CS 3D-printable inks

Three HA/CS ink formulations consisting of HA solution (5% w/v) and CS (5, 12.5 and 25% w/v) were screened for printability. Preliminary assessments were performed by qualitative observation of the ink extrudability/consistency and the shape fidelity/structural integrity of a printed monophasic test ring construct (15 mm diameter and 0.5 mm filament thickness).

Although HA alone at 5% w/v concentration exhibited poor printability (data not shown), inclusion of CS had a profound concentration-dependent effect on the architecture of the printed constructs. As shown in figure 1(A), ink 1 (5% CS) formed a construct with poor structural integrity, where deposited filaments exhibited a loose consistency. Higher shape fidelity with a more defined filament could be achieved at 12.5% CS concentration (ink 2), yet further increase of CS concentration (25%; ink 3) led to an irregular architecture due to frequent nozzle clogging and discontinuous filament deposition. Results pointed out superior extrusion-efficiency of ink 2, corroborating concentration-dependent printability of CS-based scaffolds [50].

The printability of the developed inks was quantitatively assessed via microscopical determination of the spreading ratio of the deposited filaments (figure S1), a parameter indicative of extrusion efficiency [51]. As shown in figure 1(B), ink 2 displayed the closest spreading ratio value to one ($1.13 \pm 0.01\%$), while inks 1 and 3 showed significantly higher (2.27 ± 0.02) and lower (0.6 ± 0.02) ratios, respectively, implying efficient extrudability of ink 2.

Initial viscosity values (at 25 °C and 0.012 s^{-1} shear rate) decreased significantly ($p \leqslant 0.05$) in the order of: ink 3> ink 2> ink 1> plain HA (5% w/v; figure 1(C)). Viscosity curves for the developed inks (figure 1(D)) indicated a non-Newtonian shear-thinning behavior. Both observations are of prime importance to 3D printing [52]. A relatively low viscosity ink results in the collapse of the printed construct and impaired shape fidelity, though a too viscous ink clogs the nozzle, interrupting the printing process.

Combined spreadability and viscosity data pointed to superior printability of ink 2 (5% HA w/v and 12.5% w/v CS) which was used for subsequent printing experiments involving composite inks, and henceforth referred to as plain ink.

3.1.2. Composite 3D-printable inks

3.1.2.1. Formulation

The composite NF inks contained one of the three NF formulations, namely: blank NF MS (blank MS@ink) and bioactivated MS embedding ZNP or D-ZNP (Z-MS@ink and DZ-MS@ink, respectively). In addition, two NP-loaded, non-NF composite inks incorporating free ZNP and D-ZNP (ZNP@ink and D-ZNP@ink, respectively) were included for comparison.

In our earlier work [22], we prepared Z-MS and DZ-MS as nano/microparticulate hybrid frameworks (average size of 22.2 ± 2.26 μm and 75% NP entrapment efficiency) exclusively comprising interconnecting PLA nanofibers. The MS matrix suppressed NP concentration-dependent cytotoxicity as demonstrated by cell culture studies and allowed sustained release of Zn^{2+} from both ZNP and D-ZNP. Conversely, D-ZNP endowed the nano/microconstructs with marked hydrophilicity and antibacterial activity. Additionally, they distinctly promoted the hemostatic and regenerative potentials. These hybrid nano/micro-constructs were utilized in the present

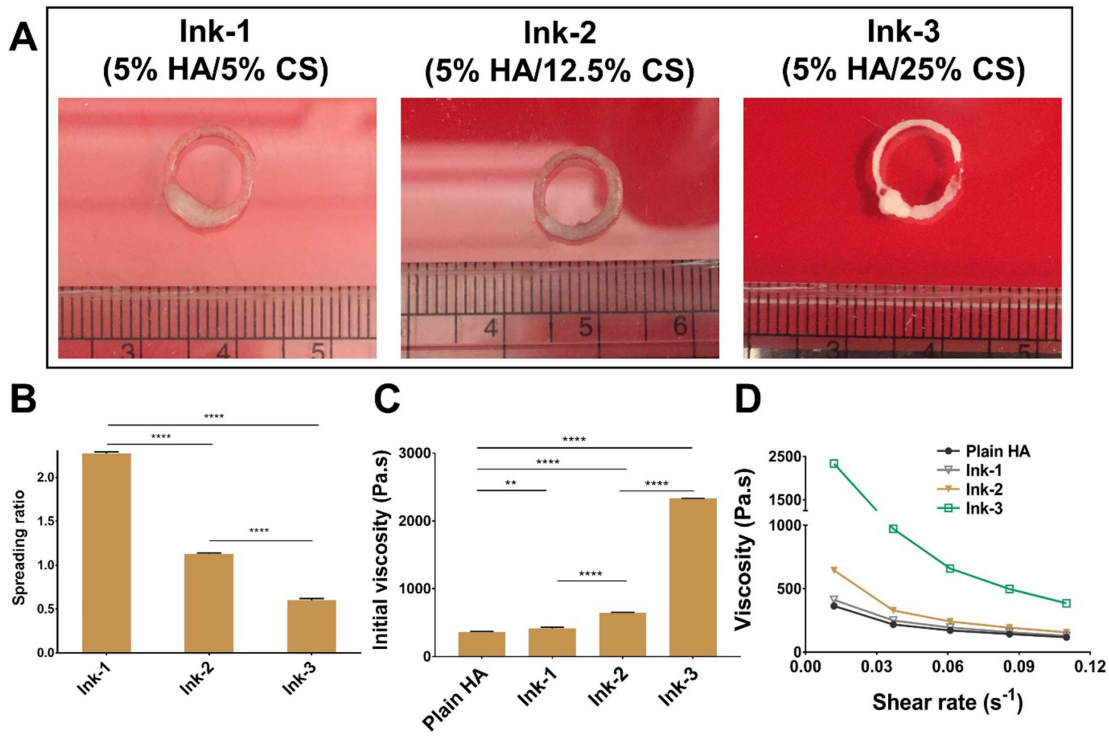

Figure 1. Development and characterization of 3D printable inks (A)–(D). (A) Printability of inks (1–3) composed of hyaluronic acid (HA) /chitosan (CS) (1:1, 1:2.5, 1:5 by weight, respectively), (B) Ink spreading ratio, $n = 5$, (C) Initial viscosity values at 0.012 shear rate and (D) Viscosity curves at 25 °C. Data represent mean ± SD, $n = 3$, $p \leqslant 0.05$. Graph asterisks denote statistical significance, * at $p < 0.05$, ** at $p < 0.01$, *** at $p < 0.001$, and **** at $p < 0.0001$.

study as injectable NF regenerative and sustained release reservoirs of ZNP and D-ZNP for the formulation of composite NF inks for the 3D printing of wound healing scaffolds.

3.1.2.2. Characterization

Composite NF inks were characterized for spreadability and rheological behavior using plain ink as control. Spreadability data (figure 2(A)) indicated that all composite inks demonstrated higher extrusion efficiency, with spreading ratio value closer to 1 (average spreading ratio 0.97 ± 0.06), compared to plain ink (1.13 ± 0.01%). NP-integration (ZNP@ink and D-ZNP@ink) showed the least effect on ink spreadability relative to plain ink. Whereas both Z-MS@ink and DZ-MS@ink presented more efficient ink extrudability. Incorporation of particulates into the gel matrix enhances the overall ink printability [53]. On the other hand, blank MS@ink presented a significantly ($p \leqslant 0.05$) lower spreading ratio (0.91 ± 0.02), which might be attributed to the relatively poor ink homogeneity caused by blank MS hydrophobicity [22] and aggregation on dispersion.

For composite inks, a significant ($p \leqslant 0.05$) increase in the initial viscosity (at 25 °C and 0.01 s^{-1}) was noted for the three NF inks, compared to plain ink and NP-composited inks (figure 2(B)). Increased viscosity can be attributed mainly to the MS structures. Likewise, inclusion of hydroxyapatite/polycaprolactone NP in gelatin-based inks was reported to increase their viscosity [40]. Viscosity curves for composite inks displayed a non-Newtonian shear thinning behavior, establishing 3D-printing convenience (figure 2(C)).

3.1.2.3. Antibacterial activity

Biomaterials used for wound healing applications should favorably possess antibacterial activity to control the infection that could impede the healing process. As *S. aureus* is amongst the most frequent organisms encountered in diabetic wounds [54], it was used to assess the antibacterial activity of the developed inks. MIC values for both plain ink and blank MS@ink are expressed in terms of NP concentration in the corresponding NP-loaded inks.

As shown in figure 2(D), control plain ink (5% w/v HA and 12.5% w/v CS) inhibited the growth of *S. aureus* at 312.5 $\mu g\ ml^{-1}$, owing to the antibacterial activity of CS [55] and HA [56]. Compositing plain ink with MS variably affected MIC values depending on the MS chemical composition. A significant ($p \leqslant 0.05$) decrease in MIC was exerted by blank MS@ink (MIC 625 $\mu g\ ml^{-1}$), possibly because of the tendency of bacterial cells to adhere to non-antibacterial NF structures, supporting bacterial growth [57]. On the other hand, Z-MS@ink and DZ-MS@ink exhibited increased antibacterial activity (MIC 19.53 $\mu g\ ml^{-1}$ and 9.76 $\mu g\ ml^{-1}$, respectively), overshadowing the effect of bacterial adherence. The present findings can be in part

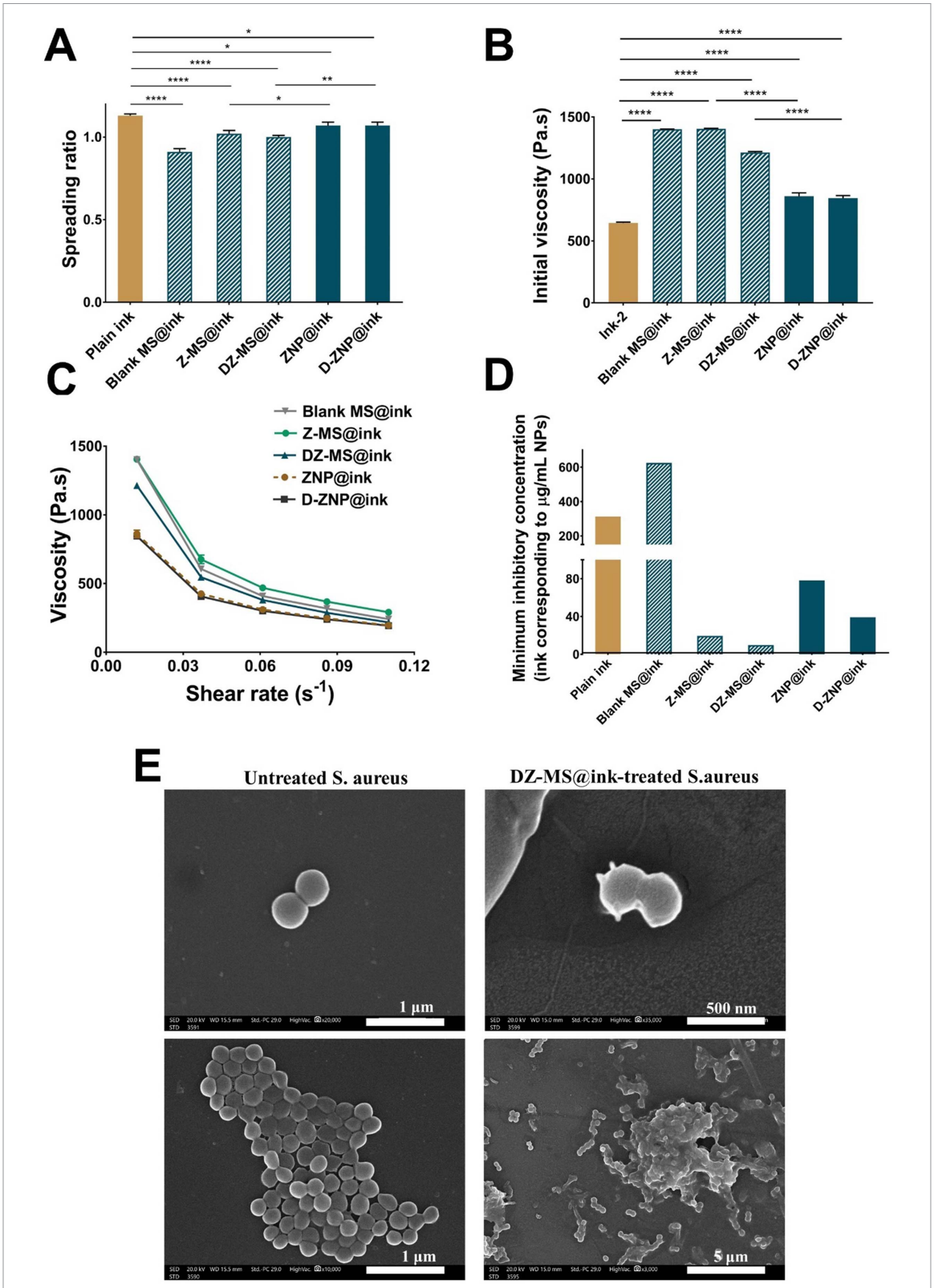

Figure 2. Development and characterization of 3D printable composite nanofibrous inks (A–E). (A) Ink spreading ratio, (B) Initial viscosity values at 0.012 s^{-1} shear rate and (C) Viscosity curves of composite nanofibrous inks at 25 °C. (D) MIC values of the test inks determined by the broth dilution method; values for plain ink and blank MS@ink are expressed in terms of NP concentration in the corresponding NP-loaded inks and (E) SEM micrographs of untreated and DZ-MS@ink-treated *S. aureus* showing morphological distortions as per treatment with one MIC of the ink at different magnifications: x20000 and x35000 (upper panel) and x3000 (lower panel). Data indicate mean ± SD, $n = 3$, $p \leqslant 0.05$, Graph asterisks denote statistical significance, * at $p < 0.05$, ** at $p < 0.01$, *** at $p < 0.001$, and **** at $p < 0.0001$.

attributed to the well-documented antibacterial activity of ZNP, reported to be further enhanced by DDAB surface treatment [34]. In addition, we have reported earlier that DDAB treatment reduces the size and increases the zeta potential of ZNP [22], which may account for the lower MIC value of D-ZNP@ink (39.06 μg ml^{-1}) compared to ZNP@ink (78.125 μg ml^{-1}). The high antibacterial activity of Z-MS@ink and DZ-MS@ink cannot be solely justified by the activity of their nanomaterial components. Indeed, ZNP@ink and D-ZNP@ink exhibited significantly ($p \leqslant 0.05$) lower activity than their respective MS-based inks (figure 2(D)). This pointed out a significant contribution of the MS NF network and possibly the HA/CS matrix to the marked activity of both Z-MS@ink and DZ-MS@ink against *S. aureus*. ZNP exhibit their significant antimicrobial activities mainly via interaction with bacterial surface, uptake by bacterial cells and release of Zn^{2+} [58]. Immobilization of ZNP and D-ZNP on PLA MS was shown to reduce their antibacterial activity despite the increase in the dissolution rate of Zn^{2+} in aqueous dispersions [22]. Incorporation of Z-MS and DZ-MS in the highly hydrophilic HA/CS ink might have promoted the dissolution of Zn^{2+}, via interaction with HA, in view of the weak binding of Zn^{2+} to PLA [59]. Complexation of Zn^{2+} ions by components of the medium was reported to increase the solubility of Zn^{2+}, enhancing their antimicrobial activity [58]. In this context, HA acid was reported to interact with Zn^{2+} at pH 6 [60] and to influence their release in aqueous media [61].

The impact of DZ-MS@ink, with the highest antibacterial activity, on *S. aureus* morphological features was investigated by SEM imaging (figure 2(E)). Untreated *S. aureus* presented typically regular, spherical, and grape-like morphological structure with an intact and smooth membrane. Treatment of *S. aureus* with one MIC of DZ-MS@ink resulted in shifting of the typical staphylococcal morphology to crumpled, irregular and aggregated cells with rough surface showing obvious signs of membrane rupture, eventual cell lysis and protoplasmic leakage. Such detrimental effects can be assigned to the bactericidal action of DZ-MS in addition to the antibacterial effect of the CS component of the ink. As such, the marked antibacterial activity of the composite NF Z-MS@ink and DZ-MS@ink strongly verified their potential for infected wound healing applications.

3.2. Optimization of crosslinker concentration

Adequate mechanical strength of scaffolds developed via extrusion-based 3D printing for tissue regeneration can be achieved by various crosslinking methods [62]. However, excessive crosslinking may result in poor nutrient transport and ECM interaction in addition to delayed degradation, all impeding neotissue development [63]. Thus, crosslinker type and concentration should be selected to maintain the balance between essential biological processes and adequate degradation rate of the scaffold [64].

In the present study, acetic acid was used as crosslinker, acting by protonating CS, promoting polyelectrolyte complexation with HA [37]. For optimization of acetic acid concentration, monophasic cylindrical/disc constructs (15 mm diameter and 2.5 mm height) were plotted using plain ink. Crosslinking was conducted by spraying the constructs with acetic acid solutions of 2, 4, 6, and 8% v/v concentration [40]. The structural integrity and resistance to liquefaction of the crosslinked 3D-printed freeze-dried scaffolds was monitored upon incubation in deionized water at 37 °C by determining the percentage swelling. Constructs crosslinked with 2% v/v acetic acid underwent fast liquefaction and collapse in one day (figure S2), while those crosslinked with higher acetic acid concentrations maintained structural integrity. Maximum swelling was attained at 2 d (432.42 $\pm$ 6.07%, 416.98 $\pm$ 2.62%, and 409.73 $\pm$ 12.87% for 4%, 6% and 8% acetic acid, respectively). Thus, a 4% acetic acid solution was considered suitable for crosslinking scaffolds in subsequent studies. The use of 4% acetic acid solution increased the ink initial viscosity from 645.2 $\pm$ 7.07 Pa.s to 4024 $\pm$ 7.07 Pa.s), verifying the selected crosslinking parameters.

3.3. 3D printing of customizable bioinspired scaffolds

3.3.1. Design of 3D-printed composite scaffolds

For 3D printing scaffolds, a bioinspired bilayer design was adopted, mimicking skin epidermal and dermal layers. As shown in figure 3(A), plain ink was used for printing the top dense layer, while composite inks (containing the equivalent of 1.25% NP) were employed for the bottom layer, giving rise to blank MS@scaffold, Z-MS@scaffold and DZ-MS@scaffold as well as their NP-integrated controls, ZNP@scaffold and D-ZNP@scaffold. Therefore, scaffolds contained an overall of 1% ZNP as the final effective antibacterial concentration, as previously reported [53]. Plain scaffolds were also 3D printed as control using plain ink for both top and bottom layers. For further customization, the bottom layers porosity was varied by modifying ink flow during printing. D-ZNP@scaffold and DZ-MS@scaffold were printed at 75% ink flow, while 100% ink flow was employed for all other scaffolds. This introduced an extra factor of macroscale porosity added to the freeze-drying induced microporosity and the nano-porosity imparted by the NF structures, giving rise to a hierarchical porosity pattern. The porosity of DZ-MS@scaffold and its control D-ZNP@scaffold was increased to boost their overall wound healing performance, anticipated from the outstanding antimicrobial activities of their respective inks.

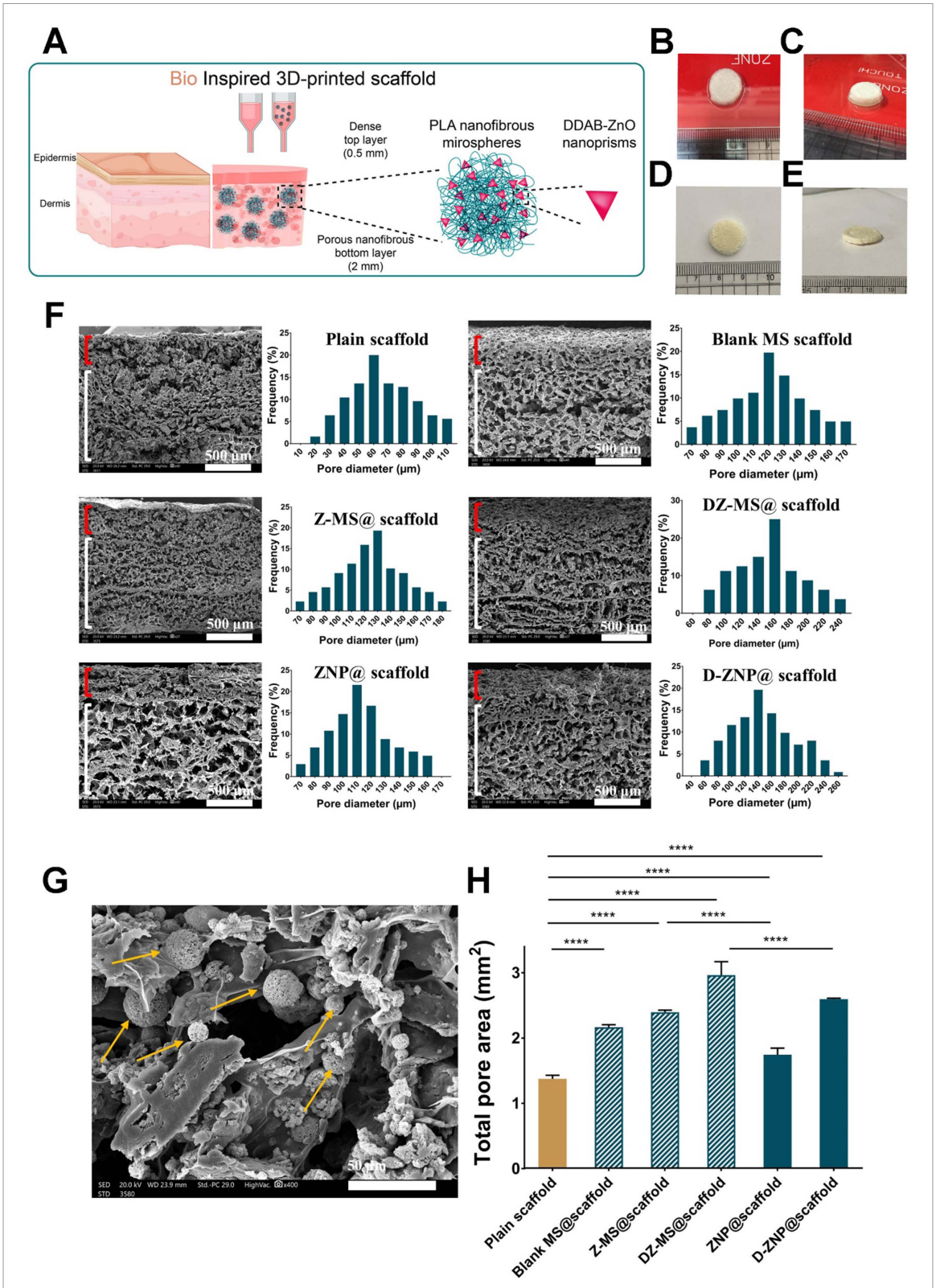

Figure 3. 3D printed bilayer scaffolds (A–H). (A) Schematic diagram for the developed, bioinspired composite DZ-MS@scaffold and representative images for (B) and (C) as-prepared and (D) and (E) freeze-dried scaffolds, at top and side view, respectively. (F) Scanning electron micrographs (SEM) of all the developed scaffolds and the pore size distribution of plain scaffold and the bottom layers for particle-loaded scaffolds. Demarcation of top layers (red brackets) and bottom layers (white brackets) can be distinguished. (G) Representative SEM of the bottom layer of Z-MS@scaffold, the arrows indicate embedded Z-MS. Scale bars for $A = 500$ μm and for $B = 50$ μm, and (H) total pore area of the bottom layers of the developed scaffolds. Data indicate mean $\pm$ SD, $n = 50$ measurements, Graph asterisks denote statistical significance, * at $p < 0.05$, ** at $p < 0.01$, *** at $p < 0.001$, and **** at $p < 0.0001$.

Scaffolds exhibited a cylindrical, disc-shaped architecture, 15 mm diameter and 0.5 mm and 2 mm top and bottom-layer heights, respectively, with different densities. The top dense layer acted as a protective barrier against mechanical irritation and wound contamination while the bottom layer served as a less compact, antibacterial/regenerative composite matrix (figures 3(B)–(E)).

3.3.2. Characterization of the 3D printed bioinspired scaffolds

3.3.2.1. SEM

Scaffolds morphological and microstructural features have a remarkable influence on their biological functionalities including cell adhesion, migration, proliferation and ingrowth [50]. Micrographs of all the developed scaffolds (figure 3(F)) revealed noticeable interconnected porosity and distinctive surface roughness. Scaffolds intrinsic porosity is possibly the result of restricted polymer chain movement imparted by freeze-drying [65]. Images verified the successful fabrication of the bioinspired bilayer scaffolds design of different porosities, with a dense top layer and a more porous and looser bottom layer. Composite MS-loaded scaffolds revealed intact MS homogenously dispersed within the scaffold bottom layer (figure 3(G)). Multilevel nano/micro porosity of these hybrid structures may promote cell adhesion, improving cell growth and proliferation [66]. In addition, scaffold porosity would allow nutrient transport, gaseous exchange, and removal of metabolic waste considered essential for skin tissue regeneration [67].

Regarding pore size distribution, the top denser layer of all scaffolds displayed relatively small pores of more or less similar size (mean 58.37 ± 19.79 μm; figure S3), matching the pore size for plain scaffold (mean 65.23 ± 21.93 μm). However, the bottom layer exhibited larger pores of different mean size: ranging from 113.19 ± 22.35 to 153.52 ± 40.58 μm (figure 3(F)). The larger pore size of the NP and MS-loaded lower layers is due to the formation of anchor points within the polymeric matrix, further restricting polymer chain movements upon freeze drying resulting in larger pores [40, 65].

Results of total pore area (figure 3(H)) indicated a significantly ($p \leqslant 0.05$) larger porosity for DZ-MS@scaffold (2.96 ± 0.21 mm^2) and its respective non-NF D-ZNP@scaffold (2.59 ± 0.01 mm^2) than other scaffolds. Both DZ-MS@scaffold and D-ZNP@scaffold were printed at a lower ink flow (75%). Thus, modulation of the ink flow may provide for scaffold customization via introducing different levels of porosity.

3.3.2.2. Mechanical properties

Scaffolds for regenerative healing of cutaneous wounds should secure adequate mechanical strength for maintaining structural stability and porosity essential for tissue regeneration [68]. Simultaneously, they should be sufficiently elastic to provide mechanical support for regenerated tissue and adapt to the natural skin stretching during the normal body movement [69]. The developed scaffolds were characterized for Young's modulus and ultimate strength as parameters indicative of deformation ability and mechanical strength, respectively.

Both Z-MS@scaffold and DZ-MS@scaffold demonstrated the highest mechanical features (figures 4(A) and (B)), though the increase was less significant ($p \leqslant 0.05$) for DZ-MS@scaffold. This could be linked to the higher porosity of DZ-MS@scaffold. Structure porosity and pore size were shown to reduce the mechanical strength of 3D-printed scaffolds [70].

Compared to NP-integrated scaffolds (ZNP@scaffold and D-ZNP@scaffold), blank MS@scaffold presented higher mechanical properties, verifying the much greater contribution of the MS than the NP components to the observed increase in Young's modulus (figure 4(A)). An approximately similar trend was observed for ultimate strength data (figure 4(B)). Polymer non-fibrous MS as well as fragmented NF structures were reported to enhance the mechanical properties of 3D printed scaffolds [62], supporting the behavior of Z-MS@scaffold and DZ-MS@scaffold. On the other hand, the higher Young's modulus and ultimate strength values of Z-MS@scaffold and DZ-MS@scaffold than blank MS@scaffold reflected the relative contribution of their respective NP components. However, the difference in size and nature of the two NP structures and their interaction with the 3D printing ink together with the design-induced porosity may account for the different mechanical features for both scaffolds.

Taken together, the developed NF composite scaffolds exhibited adequate mechanical functionalities and could thus provide the necessary structural features for hosting cellular activities for prospective wound healing.

3.3.2.3. Swelling behavior

For wound healing applications, scaffolds should ideally be able to absorb excessive wound exudate to prevent tissue maceration that hinders the healing process. Moreover, scaffolds with high water uptake ability favor cell adhesion and migration and allow nutrients transport within scaffolds which is essential for cell proliferation [71].

All composite scaffolds displayed similar swelling profiles characterized by maximum percentage swelling attained at 4 h and sustained for 72 h. This was followed by a marked decline attributed to disintegration and erosion of the scaffolds (figure 4(C)). The maximum percentage swelling was relatively high for all scaffolds (447.57 ± 4.8–881.11 ± 1.92% after 4 h) owing mainly to the hydrophilic nature of the HA/CS

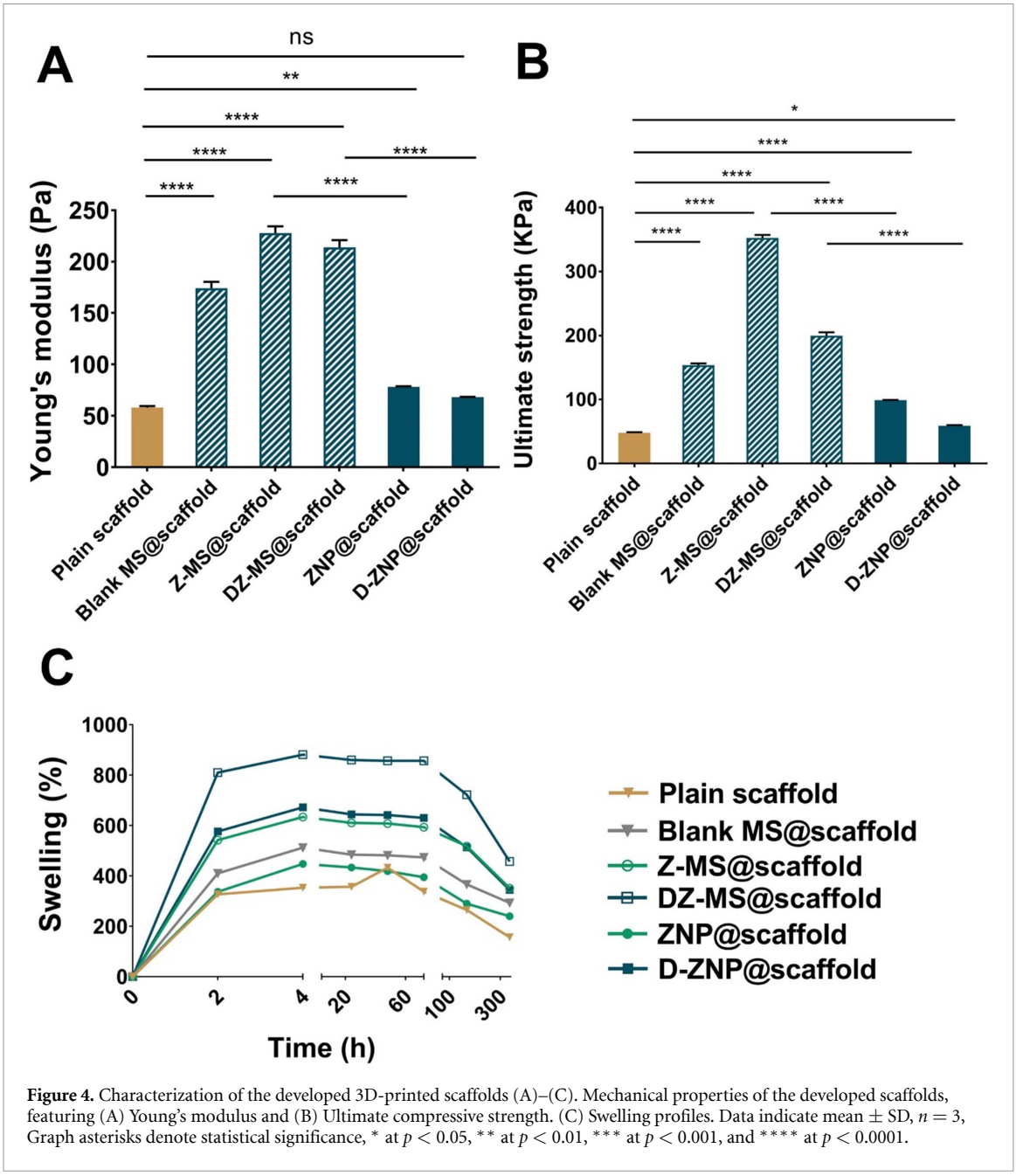

Figure 4. Characterization of the developed 3D-printed scaffolds (A)–(C). Mechanical properties of the developed scaffolds, featuring (A) Young's modulus and (B) Ultimate compressive strength. (C) Swelling profiles. Data indicate mean ± SD, $n = 3$, Graph asterisks denote statistical significance, * at $p < 0.05$, ** at $p < 0.01$, *** at $p < 0.001$, and **** at $p < 0.0001$.

hydrogel matrix, where HA entangled polymeric network allows for high water penetration [72]. Besides, the dried state of scaffolds upon freeze-drying possibly resulted in a pronounced water uptake potential [40]. It can also be noted that the percentage swelling for all scaffolds mirrored the pattern for total pore area (figure 3(H)). For instance, DZ-MS@scaffold having the largest total pore area (2.96 ± 0.21 mm^2) exhibited a higher percentage swelling compared with the less porous Z-MS@scaffold. This association verified dependence of water uptake on scaffold physicochemical properties and porosity [73]. Accordingly, relatively higher water uptake ability of the scaffolds with maintenance of their structural stability qualified them for biomedical applications, particularly wound healing.

3.3.2.4. FTIR

Infrared spectra were obtained for the crosslinked inks, their respective individual components, and physical mixtures to identify functional groups and investigate possible changes following crosslinking (figure 5(A)). The FTIR spectra of the ink matrix components CS and HA showed material-characteristic peaks. CS powder showed characteristic peaks at 1650 cm^{-1} and 1590 cm^{-1} corresponding to the amide band I (N–H bending of residual N-acetyl group) and amide band II (N–H vibration of primary amine groups), respectively. In addition, an intense broad band was recorded in the range of 3500 cm^{-1} to 3000 cm^{-1}, corresponding to the O–H and N–H stretching vibration. The absorption band at 2871 cm^{-1} was assigned to the stretching vibration

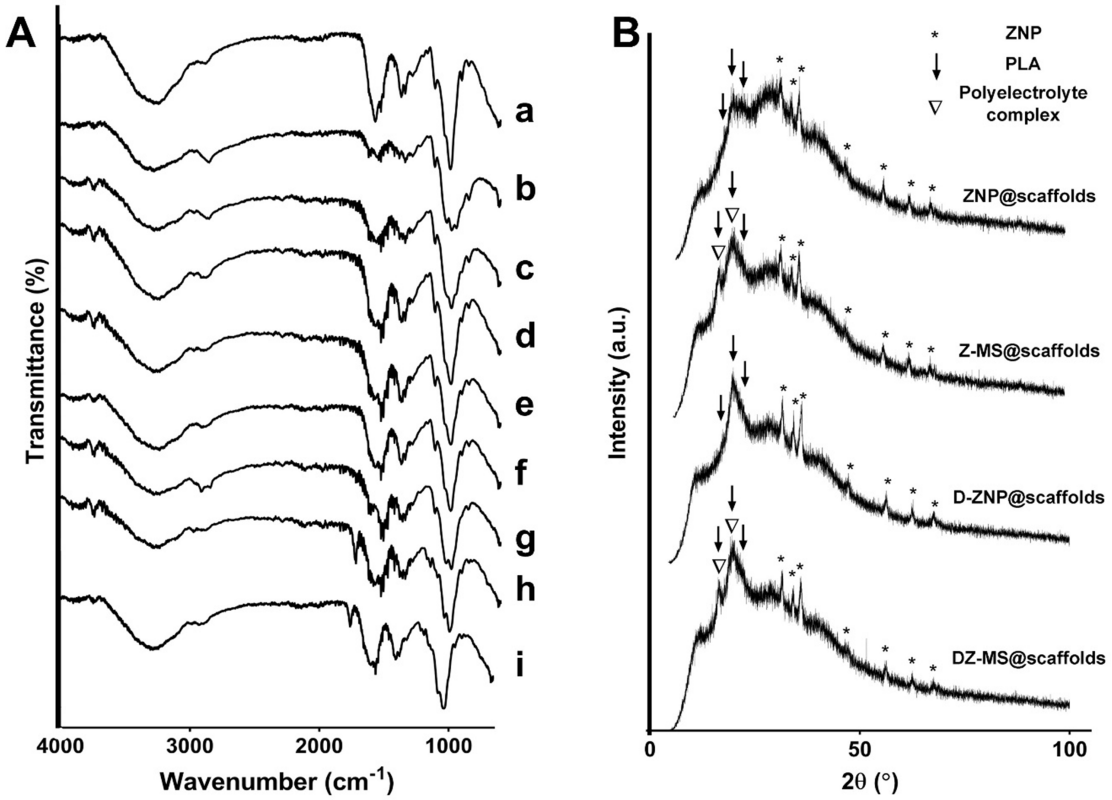

Figure 5. Physicochemical characterization of the developed scaffolds (A) and (B). (A) Fourier transform infrared spectroscopy (FTIR) charts: HA (a), CS (b), HA and CS mixture (c) and crosslinked inks for plain scaffold (d), ZNP@scaffold (e), D-ZNP@scaffold (f), blank MS@scaffold (g), Z-MS@scaffold (h) and DZ-MS@scaffold (i), and (B) x-ray diffraction patterns (XRD) of the developed scaffolds showing peaks of individual components.

of -CH_2-. Also, peaks at 1155 cm^{-1} and 897 cm^{-1} were related to the asymmetric vibrations of C–O–C and were representative of the saccharide structure [74]. The HA spectrum showed characteristic peaks at 1620 cm^{-1} and 1415 cm^{-1}, assigned to the asymmetric and symmetric stretching vibration of the carboxylate group, respectively, while the amide band II was recorded at 1556 cm^{-1}. In addition, the absorption bands at 2880 cm^{-1} and 1321 cm^{-1} were related to C–H and C–N stretching, respectively [37].

Regarding 3D-printed crosslinked scaffolds, the band recorded at 1570 cm^{-1} corresponding to the bending vibration of the protonated amine group (NH^{3+}) of CS verified successful crosslinking of CS and HA [75]. The FTIR spectra of all composite scaffolds revealed the same characteristic peaks of their respective particulate MS or NP components reported earlier [22]. Additionally, the lack of new peaks in the spectra of particle-loaded scaffolds verified the absence of any newly formed chemical bonds. Finally, FTIR spectra of physical mixtures exhibited the characteristic peaks of their individual components (figure S4).

3.3.2.5. XRD analysis

XRD analysis was conducted to assess the overall crystallinity of composite particle-loaded scaffolds. As can be seen in figure 5(B), the XRD spectra of all test scaffolds retained the characteristic peaks of ZNP at 2θ of 31.6°, 34.2°, 36.1°, 47.4°, 56.5°, 62.8°, 67.8°, and 69.0°, corresponding to the (100), (002), (101), (102), (110), (103), (112), and (201) crystal planes, respectively [22]. Additional peaks assigned to PLA were noted for MS-loaded scaffolds at $2\theta = 16.8°$ and 19.0°. Results confirmed successful incorporation of ZNP and D-ZNP within the respective composites while conserving their crystalline structure. XRD diffractograms of composite scaffolds also revealed diffraction peaks at around $2\theta = 14.17°$, 17.31°, 19.05° and 22.56°, possibly associated with the polyelectrolyte complex formed by the electrostatic interaction between CS and HA [76], which further verified successful crosslinking. It is worth mentioning that the broad hump observed for all peaks might be attributed to the high polymeric content, possibly overlapping with the characteristic peaks of NP and MS, resulting in a noticeable decrease in the intensity of their peaks [65].

3.4. Wound healing studies in rats

Wound healing is a highly specialized dynamic process that takes place according to overlapping hemostasis, inflammation, proliferative and remodeling phases mediated by the interaction of several types of cells, growth factors and cytokines [77]. However, the healing of diabetic wounds is generally impaired

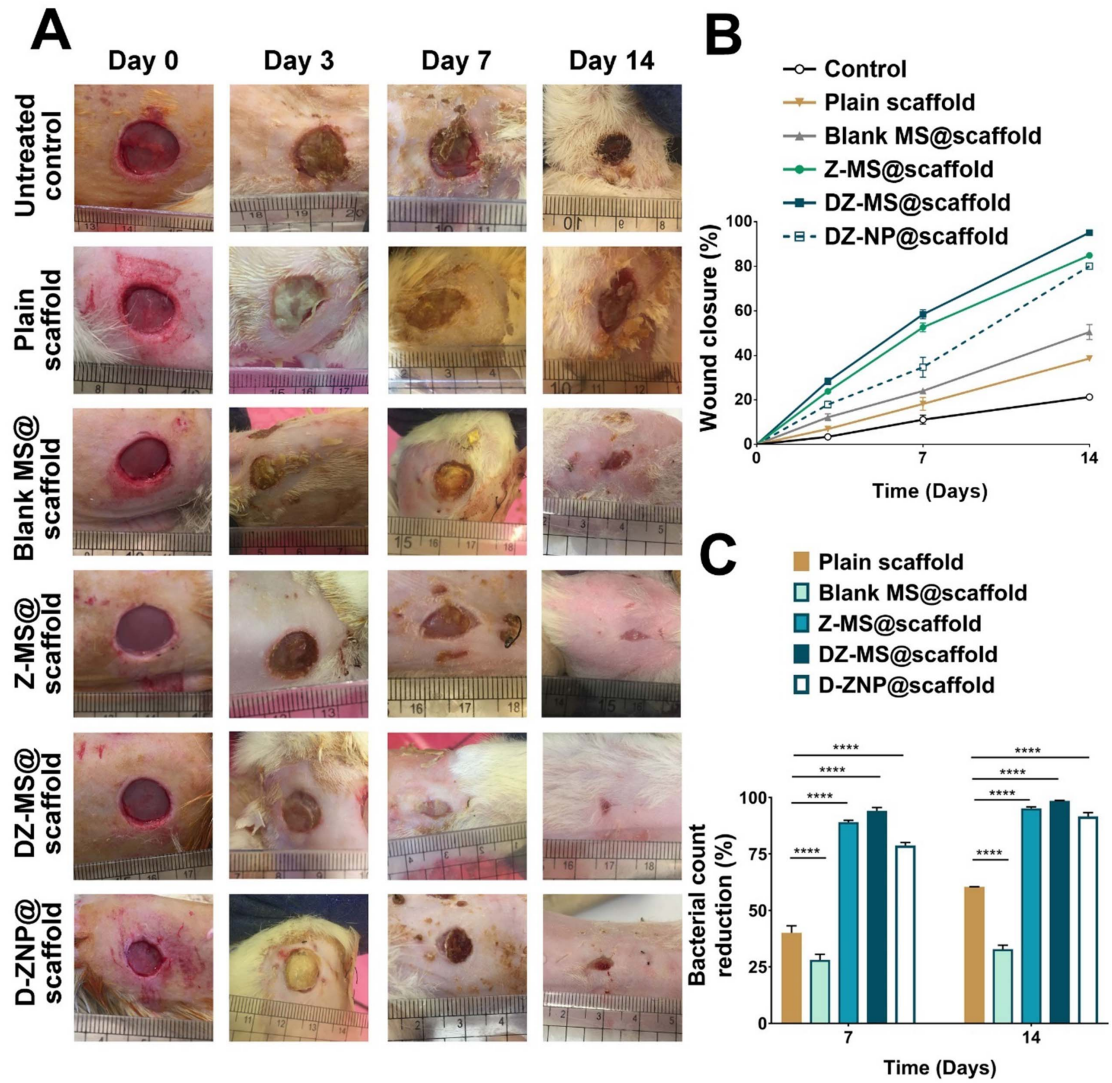

Figure 6. Wound healing in infected diabetic wounds (A)–(C). (A) Representative images in different groups on days 0, 3, 7, and 14 post surgery, (B) Percentage wound closure for chronic wounds in different groups, and (C) percentage reduction of *S. aureus* in different groups on days 7 and 14 post surgery. Data indicate mean ± SD, $n = 4$, Graph asterisks denote statistical significance, * at $p < 0.05$, ** at $p < 0.01$, *** at $p < 0.001$, and **** at $p < 0.0001$.

by a complex pathophysiology involving vascular, biochemical, neuropathic, immune and infection components [78]. Wound healing studies were initiated following successful induction of the diabetic state (figure S5). The healing/regenerative/antibacterial efficacy of the developed 3D-printed bilayer composite NF scaffolds, Z-MS@scaffold and DZ-MS@scaffold, was assessed in comparison with their component scaffolds using full thickness excision infected diabetic wounds in rats as a model of chronic wounds. In addition, a non-diabetic acute wound model was employed for evaluating the ability of Z-MS@scaffold to accelerate the healing of full thickness excision non-diabetic acute wounds.

3.4.1. Wound closure

Representative digital images of the healing progress of chronic wounds at days 3, 7 and 14 post surgery are shown in figure 6(A) while respective percentage wound closure and percentage bacterial count are shown in figures 6(B) and (C), respectively. Untreated control wounds failed to heal throughout the study (figure 6(A)), with 21.36 ± 1.35% closure attained by day 14 (figure 6(B)), verifying successful establishment of a hard-to-heal wound model in the diabetic rats. All the employed scaffolds achieved significantly ($p \leqslant 0.05$) higher percentage wound closure than the untreated control groups for all time points. Plain scaffold achieved 38.62 ± 0.47% wound closure by day 14 (figure 6(B)). Healing improvement can be ascribed to the scaffold porosity (total pore area 1.38 ± 0.05 $mm^{2;}$ figure 3(H)) and CS-induced antibacterial activity (40.07 ± 3.13% and 60.43 ± 0.05% bacterial count reduction at the 7- and 14 day time points, respectively) (figure 6(C)). Indeed, a drug free HA/CS combination scaffold was recently shown to synergistically heal infected diabetic wounds in a murine model [33].

Besides, the protective/porous scaffold bilayer structure (total pore area 1.38 ± 0.05 $mm^{2;}$ figure 3(H)) of the scaffold might have also contributed to healing enhancement.

Compositing the HA/CS hydrogel scaffold with blank MS (blank MS@scaffold) resulted in further healing improvement throughout the study, achieving 50.51 ± 3.38% wound closure at day 14 (figure 6(B)). These results highlighted the superior regenerative functionality of the ECM-mimicking NF structure imparted by MS. Inclusion of MS into the porous hydrogel scaffold generated a complex structure with multilevel porosity (figure 3(A)). Interactive motifs of such complex structures offer cellular cues for a regenerative microenvironment [79]. Nevertheless, blank MS@scaffold exhibited a lower antibacterial effect (32.84 ± 1.83% count reduction at day 14; figure 6(C)) than plain scaffold. Non-antibacterial NF matrices tend to promote bacterial growth because of their large surface area and high porosity [57].

Composite Z-MS@scaffold resulted in significant ($p \leqslant 0.05$) healing enhancement at all time points, achieving 84.96 ± 0.31% wound closure at day 14 (figure 6(B)), pointing out the prominent contribution of the ZNP component to the healing process. These results can be in part attributed to the enhanced swelling properties of Z-MS@scaffold (figure 4(C)) and early antibacterial action (89.13 ± 0.79% and 95.21 ± 0.71% bacterial reduction at days 7 and 14, respectively; figure 6(C)). We have demonstrated earlier that ZNP exert an early bactericidal effect against *S. aureus* species. As no studies have been reported to date on the wound healing efficacy of 3D printed ZNP-functionalized scaffolds, the current findings provide information on an alternative customizable biomaterial featuring different porosity/topography with good wound healing prospectives. Though results are strikingly good, there is room for improvement.

To maximize the healing efficacy of the Z-MS@scaffold, compositional and structural customization was undertaken. This was achieved via scaffold bioactivation with DZ-MS at non-cytotoxic DDAB concentration based on our reported cell culture data [22] and increasing scaffold porosity via 3D-printing at 75% ink flow. The customized DZ-MS@scaffold significantly accelerated the healing process at all time points, achieving 95.17 ± 0.03% wound closure at day 14 (figure 6(B)). Also, DZ-MS@scaffold significantly enhanced bacterial inhibition (94.13 ± 1.48% and 98.53 ± 0.23% count reduction after 7 and 14 d, respectively; figure 6(C)), probably attributed to the prominent antibacterial efficacy of DZ-MS@ink (figure 2(D)). Moreover, such improvement can be ascribed to the higher porosity and consequent increase in water uptake by DZ-MS@scaffold (figure 4(C)), resulting in a moisture-controlled wound bed. The present findings generally put forth the DZ-MS@scaffold as a promising bioactive material with distinctive wound healing potential.

To the best of our knowledge, the wound healing performance of D-ZNP has not been verified to date. This initiated evaluation of the healing properties of a simple D-ZNP@scaffold devoid of MS to pinpoint the contribution of MS to the healing process. Despite an appreciable healing effect, the D-ZNP@scaffold was significantly ($p \leqslant 0.05$) less effective than the DZ-MS@scaffold in terms of wound closure (80.12 ± 0.21% at day 14; figure 6(B)) and infection suppression (figure 6(C)). This clearly pointed out the favorable impact of the MS multifunctionality on D-ZNP performance. Indeed, D-ZNP@scaffold lacks the distinctive ECM-mimicking structure of MS, their water uptake (figure 4(C)) and the MS-induced antibacterial activity enhancement of D-ZNP (figure 2(D)). Furthermore, the D-ZNP@scaffold was devoid of the MS large surface area necessary for massive embedding of D-ZNP and effective sustained release of Zn^{2+}. This potentially reduced the continued *in situ* availability of D-ZNP and Zn^{2+} in the wound milieu. Integrating biomaterials greatly enhances the performance of inorganic NP as diabetic wound healing promotors in both *in vitro* and *in vivo* studies provided that cytotoxicity is controlled [80].

The relatively lower chronic wound healing efficacy of Z-MS@scaffold relative to DZ-MS@scaffold initiated the appraisal of Z-MS@scaffold for treating less challenging non-diabetic acute wounds. Untreated control acute wounds showed progressive healing, attaining 76.64 ± 1.04% closure at 14 day (figure 7(A)). Spontaneous self-healing and regaining of structural integrity of untreated acute wounds is generally mediated by the skin ability to promote overlapping wound healing phases and dynamically coordinate cellular responses and growth factors [77]. Healing was significantly ($p < 0.05$) accelerated by Z-MS@scaffold at all time points, achieving almost complete wound closure (96.69 ± 0.35%) by day 14 (figure 7(B)), an outcome of benefit to patients with acute wounds.

Wound closure data (post hoc power analysis = 100%) provided evidence for the aptness of Z-MS@scaffold for accelerating the healing of simple non-diabetic wounds and the superiority of DZ-MS@scaffold in treating diabetic chronic wounds.

3.4.2. Histological examination and histomorphometric analysis of wound microstructure

A histological and histomorphometric investigation was undertaken to substantiate wound closure evaluation. Representative photomicrographs of diabetic wound sections are shown in figures 8(A)–(F) while values for inflammatory scores and fibrotic indices are shown in figures 8(G) and (H), respectively.

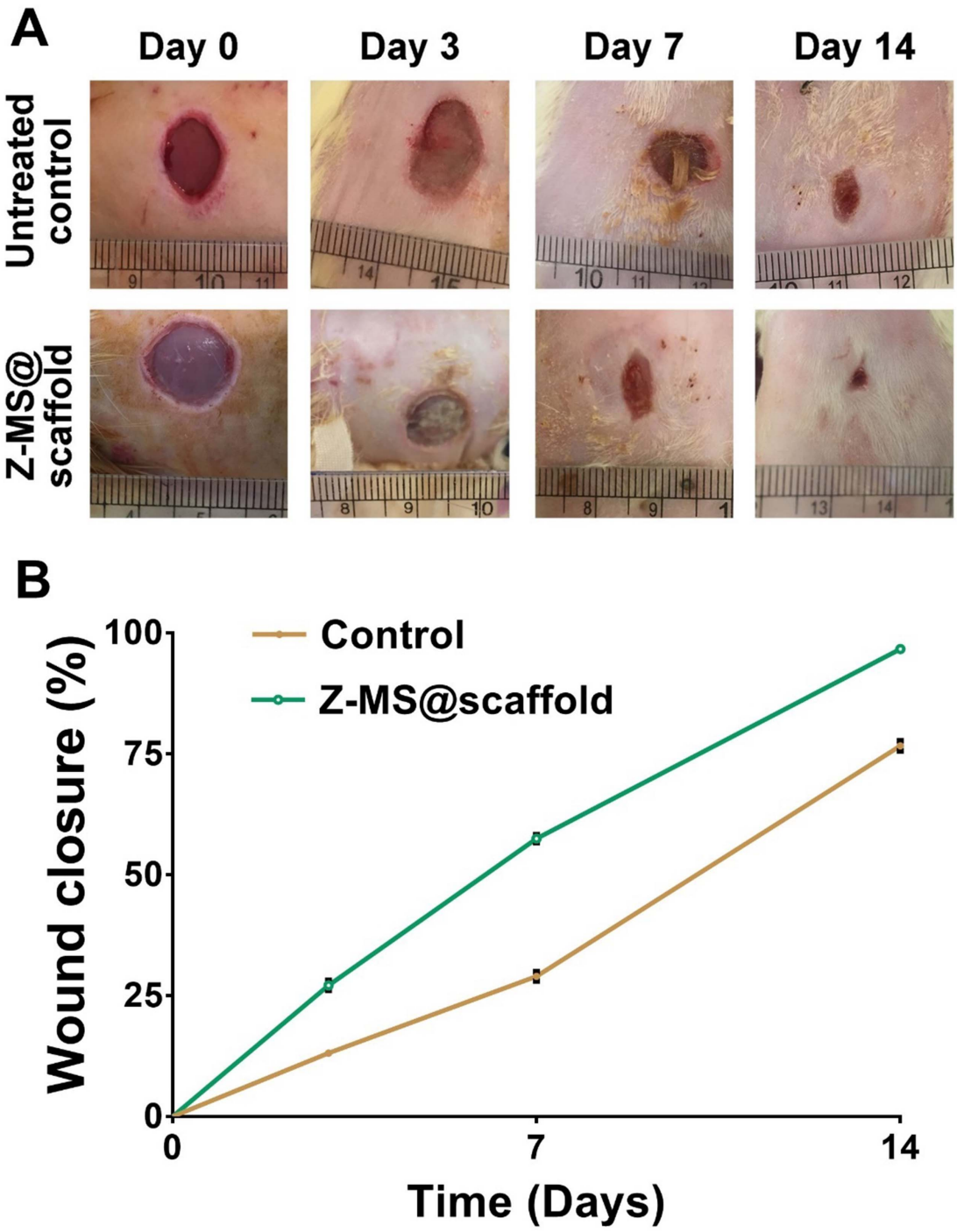

Figure 7. Wound healing in acute, non-diabetic wounds (A) and (B). (A) Representative images in different groups on days 0, 3, 7, and 14 post surgery and (B) Percentage wound closure of acute wounds in different groups. Data indicate mean ± SD, $n = 4$.

Photomicrographs for normal skin (figure S6) showed an intact epidermal surface and dermal layer with normal skin appendages, recording 21.8 ± 2.7 fibrotic index and median inflammatory score of 1. Untreated control diabetic wounds revealed retarded healing associated with ulceration of the epidermal surface and massive diffuse infiltration of chronic inflammatory cells, scoring 4 (figure 8(A)). Wound healing was attempted through fibrosis of the dermal layers, with a shooting fibrotic index of 102.4 ± 5.63 (MT-stained collagen fibers; figure 8(A)). Observations were generally consistent with morphological and morphometric assessments of untreated diabetic wounds [81].

Treatment with plain hydrogel scaffolds resulted in almost complete epithelial healing of the injured area (figure 8(B)), though with coalescent chronic inflammation (scoring 3) and fibrotic intensity of 95.9 ± 13.6. The plain scaffolds demonstrated obvious biocompatibility and biodegradation with

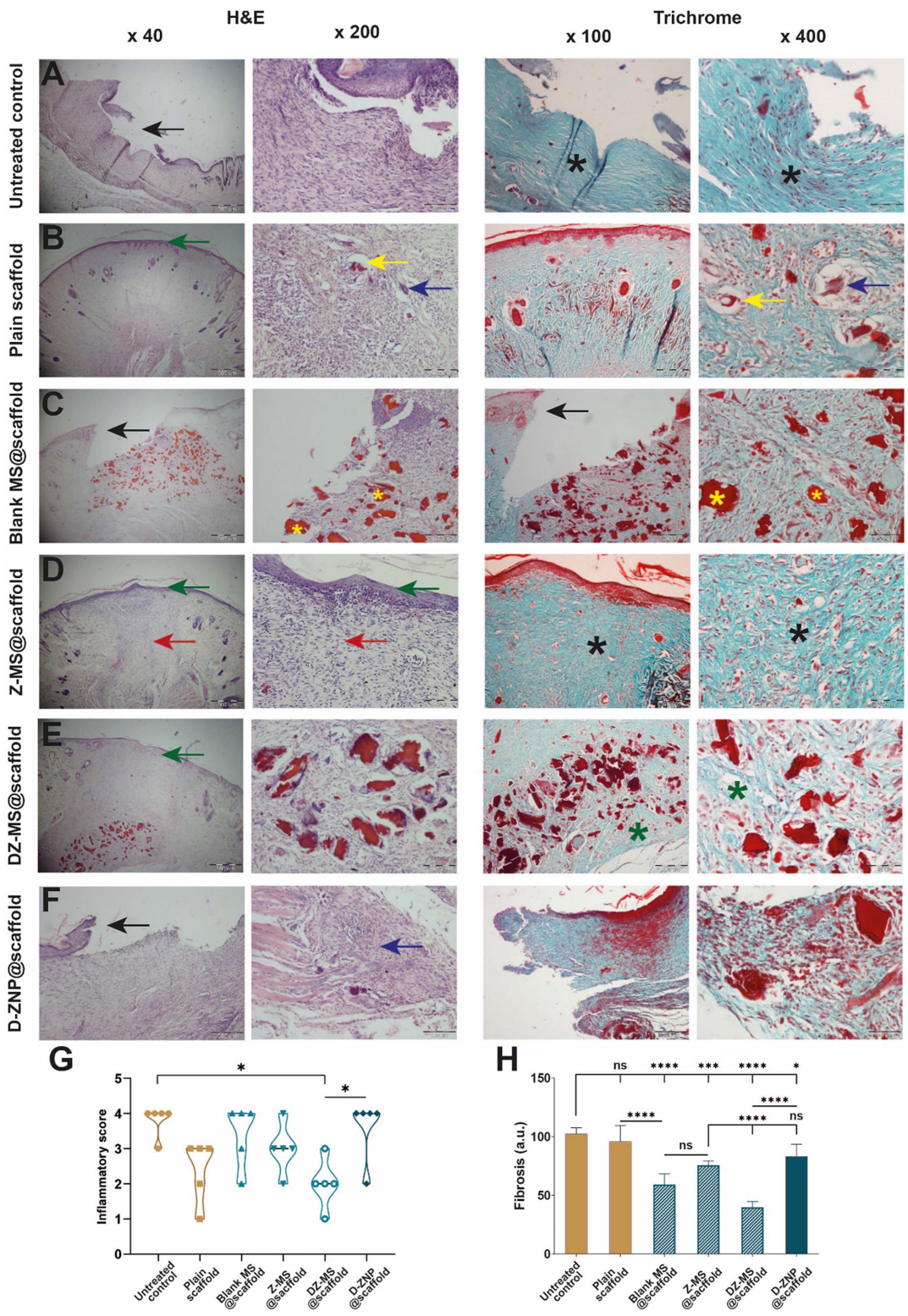

Figure 8. Histological and morphometric analysis of the diabetic, chronic wound groups (A)–(H). H&E and trichrome-stained photomicrographs for (A) the ulcerated epidermal surface (black arrow) in the untreated diabetic control wound with fibrotic dermal reaction (black asterisks). (B) The plain scaffolds group shows epithelialization (green arrow) of the injured area with granulomatous dermal immunoreaction. The blue arrows point out the foreign body multinucleated giant cells, while the yellow arrows denote scaffold remnants. (C) Blank MS@scaffold present impaired wound closure (black arrows) and delayed scaffold matrix degradation (yellow asterisks). However, they reveal reduced fibrotic dermal reaction. (D) Z-MS@scaffold promoted the epithelial healing process (green arrows) but elicited a diffuse inflammatory reaction (red arrows) with intense fibrosis (black asterisks). (E) DZ-MS@scaffold reveal complete epithelialization of the wound (green arrow) with marked reduction of the fibrotic dermal reaction (green asterisks). (F) For D-ZNP@scaffold, the wound edges failed to heal (black arrow) with granulomatous reaction (blue arrow). Scale bar 500 μm for $\times$40, 100 μm for $\times$200, 200 μm for $\times$100 and 50 μm for $\times$400. (G) The violin plot of the median inflammatory scores, showing a low score for DZ-MS@scaffold. (H) The fibrotic index (arbirtrary units; a.u.) of trichrome-stained collagen fibers, showing profound reduction of fibrosis in DZ-MS@scaffold. Data represent mean $\pm$ SD of the reciprocal intensity, $n = 5$ measurements. Graph asterisks denote statistical significance, * at $p < 0.05$, ** at $p < 0.01$, *** at $p < 0.001$, and **** at $p < 0.0001$, while ns denotes non-significance of $p > 0.05$.

the induction of multifocal deep-seated granulomatous reactions around the barely detected scaffold remnants. HA/CS hydrogels showed faster healing of diabetic wounds via an antibacterial effect associated with epidermal regeneration, collagen deposition and angiogenesis [33, 82].

Blank MS@scaffold treatment did not achieve wound closure. Degradation of the scaffold resulted in diffuse granulomatous reactions around the scaffold remnants and the formation of foreign body multinucleated giant cells (figure 8(C)). Moreover, blank MS@scaffold elicited infiltration of inflammatory cells, raising the median inflammatory score to 4. Nevertheless, the blank MS@scaffold significantly ($p < 0.0001$) ameliorated the dermal response to mild fibrosis, recording an intensity of 59.2 ± 9.2. Blank PLA MS appear to have interfered with the degradation of the HA/CS hydrogel matrix despite their NF structure. This can be explained by the relatively slow degradation of PLA under physiological conditions. PLA hydrophobicity and crystallinity delay initiation of the hydrolytic degradation reaction [83].

Z-MS@scaffold achieved almost complete epithelialization of the diabetic wound, except for a small area showing acute inflammatory infiltrate (figure 8(D)). However, the scaffold did not restore complete dermal structures at the wound site. This was accompanied by a severe chronic inflammatory infiltrate (scoring 3) and a noticeable fibrotic line of demarcation with 75.7 ± 3.5 RI.

Notably, customized DZ-MS@scaffold could afford complete healing of the epithelial edges with marked reduction of the fibrotic dermal reaction and restoration of the skin elasticity (figure 8(E)). The scaffold elicited a mild focally granulomatous reaction and chronic inflammatory response (scoring 2) as well as a sparsely underlying fibrotic dermal reaction (39.9 ± 4.9). Improved wound healing can be attributed to the marked water absorption capacity and antibacterial functionality enhancement by the DZ-MS component of the scaffold. This was verified by the significantly lower healing efficacy of D-ZNP@scaffold devoid of the MS carrier component (figure 8(F)). In fact, the D-ZNP@scaffold hardly promoted the healing process. Poor epithelialization and restoration of the dermal structure in addition to the induction of a granulomatous reaction were observed. Relative to plain scaffold, D-ZNP increased the inflammatory score (scoring 4 *vs* 3), though they did not significantly affect its fibrosis index (83.3 ± 10.18 *vs* 95.5 ± 13.62; $p > 0.05$). Inferior healing performance of the D-ZNP@scaffold can be attributed to the absence of MS, which were shown to enhance D-ZNP cytocompatibility and sustain the *in vitro* availability of their Zn^{2+} [22].

The potential of Z-MS@scaffold to treat non-diabetic acute wounds was assessed histologically (figures 9(A)–(D)). The untreated control group showed incomplete epithelialization of the wound ulcerative area (figure 9(A)). The healing process was delayed by an intense superficial acute inflammatory cell infiltration with a diffuse scoring 4. Fibrotic healing was reflected morphometrically by the formation of intense collagen bundles of 101.1 ± 5.7 RI, replacing the loose mature collagen fibers of the unwounded dermal skin layer (figure S6). In contrast, Z-MS@scaffold treatment resulted in full structuring of the epidermal layer and complete restoration of the dermal structures, with no signs of remaining scaffold matrix (figure 9(B)). An inflammatory score of 1 for Z-MS@scaffold indicated a deeply seated focal aggregation of mixed acute and chronic inflammatory cells without foreign body reaction (figure 9(C)). Besides, a significantly ($p < 0.0001$) lower fibrotic intensity (31.8 ± 2.1 RI; figure 9(D)) than the untreated control implied enhanced elasticity of the wounded skin to approach that of normal skin. The lower inflammatory score for Z-MS@scaffold in the treatment of acute wounds relative to chronic wounds (1 *vs* 3) and fibrosis index (31.8 ± 2.1 *vs* 59.2 ± 9.2) substantiated greater aptness of this scaffold in treating simple acute wounds. Such discrepancy highlights the need for customization of wound healing platforms with compositional and structural features offered by the inclusion of DDAB-modified ZNP-MS and the opportune adoption of tailored-3D printing adjustments.

Wound healing data indicated that the printing process-induced customization of the scaffold porosity/topography coupled with the powerful antimicrobial activity of DZ-MS could favorably orchestrate skin regeneration with mild inflammation and fibrosis, markedly enhancing treatment outcomes.

3.4.3. Quantification of healing-associated biomarkers

The inflammatory phase of wound healing is an essential innate immune response that involves tissue breakdown and cleaning of infection and debris. However, persistent inflammation in diabetic wounds results in the accumulation of inflammatory cytokines, such as TNF-α, causing tissue damage and delayed healing [84]. Elevated levels of TNF-α are followed by a decline of VEGF, thereby delaying angiogenesis and interfering with the proliferative wound healing phase. Moreover, the diabetic wound microenvironment is not generally supportive of the bioavailability and chemical integrity of local growth factors including EGF, compromising their healing accelerating effect and wound epithelialization [85]. Accordingly, we investigated the effect of the applied composite scaffolds on the levels of TNF-α via RT-qPCR and the growth factors VEGF and EGF by ELISA in wound tissues harvested 14 d post wounding.

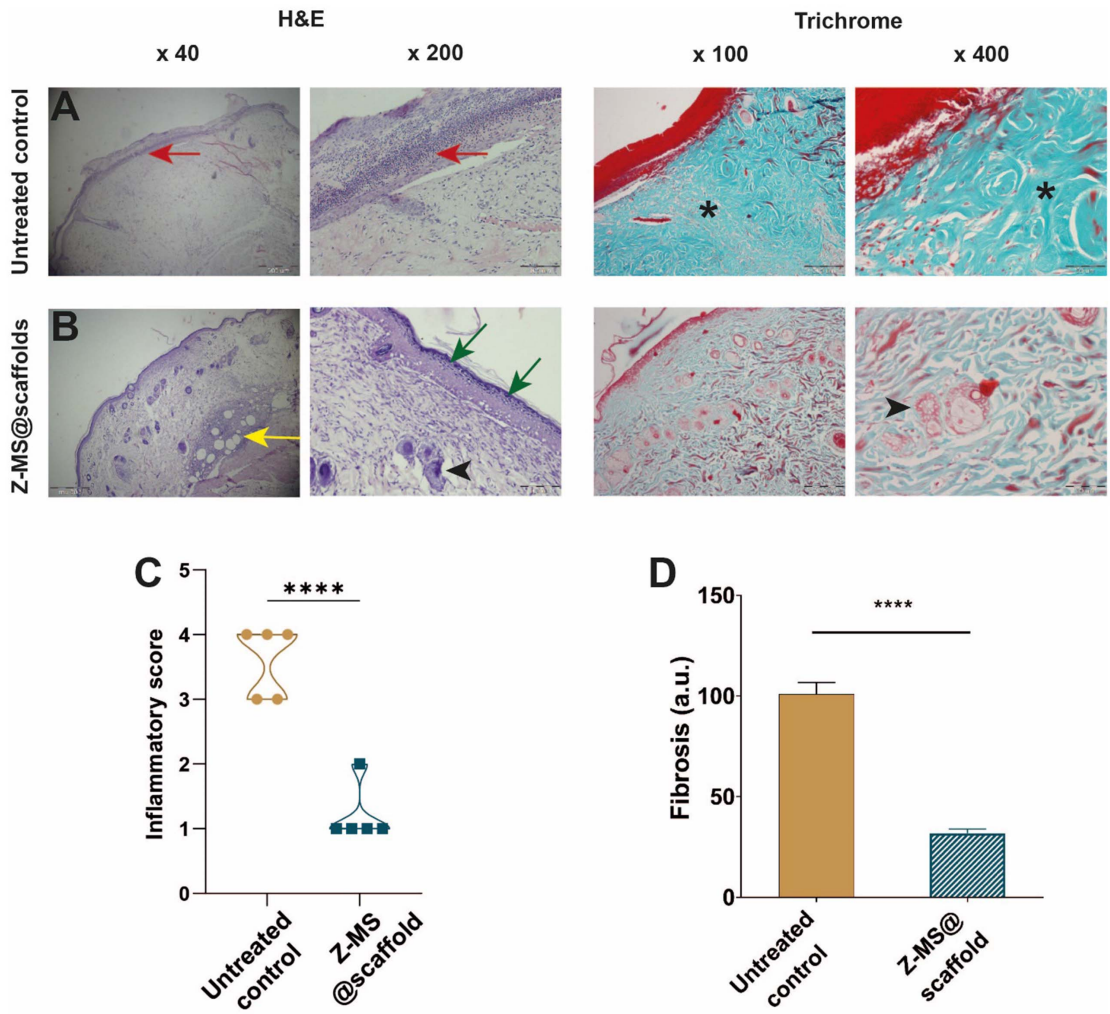

Figure 9. Histological and morphometric analysis of the acute non-diabetic wound groups (A)–(D). (H) and (E)- and trichrome-stained photomicrographs for (A) The untreated acute wound control reveals an incomplete fibrotic healing process (black asterisks) with intense neutrophil infiltration at the ulcerated epithelial edges (red arrows). (B) The Z-MS@scaffold restored skin layers: epidermally with prominent granular cell layer (green arrows) and dermally with the skin appendages (black arrowheads). The yellow arrow points out the deep-seated focal inflammatory infiltrate. Scale bars are 500 μm for $\times$40, 100 μm for $\times$200, 200 μm for $\times$100 and 50 μm for $\times$400. (C) The violin plot of the median inflammatory score, showing the low inflammation elicited by Z-MS@scaffold. (D) The bar graph of the fibrotic index, measuring the reciprocal intensity of trichrome-stained collagen fibers, where Z-MS@scaffold reveal profound reduction in fibrosis compared to untreated wounds. Data represent mean $\pm$ SD, $n = 5$ measurements. Graph asterisks denote statistical significance, ** at $p < 0.01$ and **** at $p < 0.0001$, while ns denotes non-significance of $p > 0.05$.

As shown in figure 10(A), untreated diabetic wounds indicated overexpression of TNF-α (7.02 $\pm$ 1.34-fold change). This was significantly ($p \leqslant 0.05$) decreased by the composite DZ-MS@scaffold followed by Z-MS@scaffold and to a lesser extent their component scaffolds (plain scaffold, blank MS@scaffold and D-ZNP@scaffold). These results point out the role of ZNP in regulating the wound environment and its further enhancement by DDAB treatment. It has been reported that ZNP reduced pro-inflammatory cytokines including TNF-α, promoting wound healing in the inflammation phase [86]. However, the effect of DDAB-modified ZNP on knocking down TNF-α has not been documented to date. The lower anti-inflammatory efficacy of D-ZNP@scaffold compared to DZ-MS@scaffold further verified implication of the MS carrier in enhancing the biological functionality of D-ZNP. This corroborated the results of wound closure and histopathological analyses (figures 6 and 8, respectively). Regarding non-diabetic acute wounds, the level of TNF-α was expectedly lower in untreated acute wounds than untreated diabetic wounds, confirming the higher inflammation state of diabetic wounds. Also, TNF-α levels were significantly ($p \leqslant 0.05$) downregulated by Z-MS@scaffold, affirming efficacy of the scaffold in treating acute wounds.

Results for the growth factors (figures 10(B) and (C) indicated the lowest level of both VEGF and EGF (22.5 $\pm$ 0.7 pg mg^{-1} and 31.5 $\pm$ 0.71 pg mg^{-1}, respectively) in untreated diabetic wounds, as reported [87]. The expression of both factors was significantly ($p \leqslant 0.05$) increased by the composite Z-MS@scaffold and DZ-MS@scaffold and to a

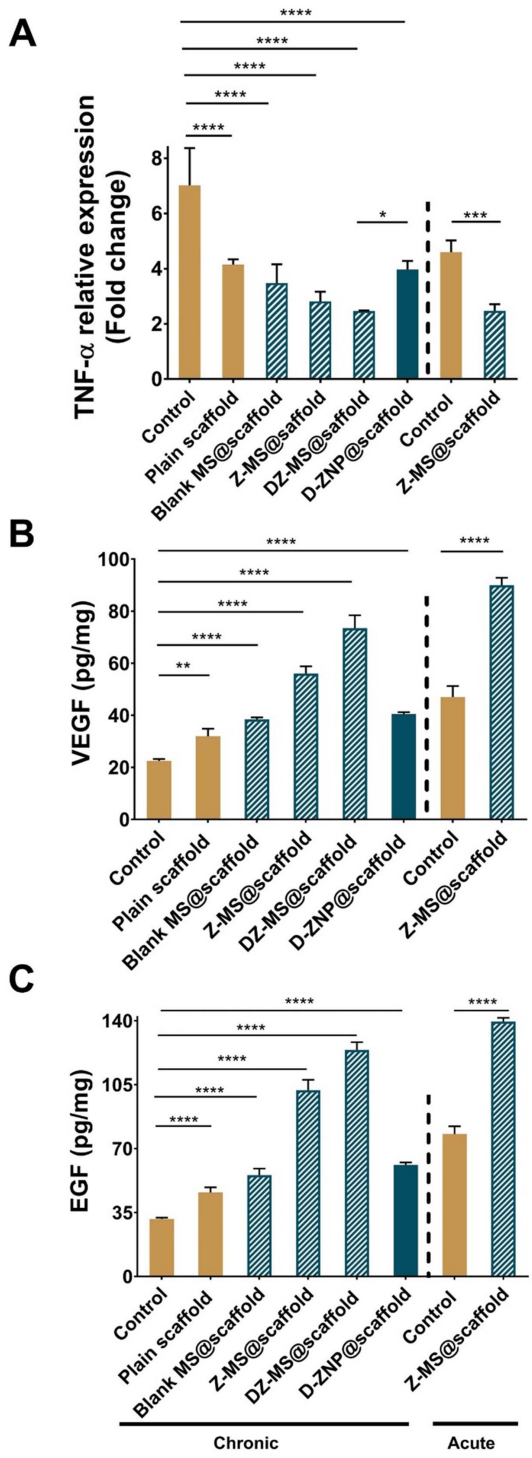

Figure 10. Quantitative analysis of healing-associated biomarkers in regenerated skin tissue for chronic and acute wounds obtained at day 14 post surgery (A)–(C). (A) Quantitative RT-PCR analysis for TNF-α gene expression and quantitative ELISA analysis of (B) VEGF and (C) EGF. Data indicate mean $\pm$ SD, $n = 4$, Graph asterisks denote statistical significance, * at $p < 0.05$, ** at $p < 0.01$, *** at $p < 0.001$, and **** at $p < 0.0001$.

lesser extent by their component scaffolds. This can possibly be attributed to the reduction of TNF-α levels, promotion of the synthesis of growth factors and/or their retention in the wound tissue. Indeed, the trend of growth factors upregulation by the test scaffolds mirrored that of TNF-α downregulation. DZ-MS@scaffold secured the highest expression of both VEGF and EGF (73.5 $\pm$ 4.95 pg mg^{-1} and 124 $\pm$ 4.24 pg mg^{-1}, respectively) followed by Z-MS@scaffold (56 $\pm$ 2.83 pg mg^{-1} and 102 $\pm$ 5.66 pg mg^{-1}, respectively). ZNP are known to upregulate pro-angiogenic factors such as the VEGF by the generation of reactive oxygen species [88], supporting capillary regeneration and improving oxygen and nutrient supply at wound site. Moreover, the ZNP-induced increase in EGF level implied contribution of ZNP to the proliferation of epithelial cells and fibroblasts, and wound epithelialization. Although DDAB modification of ZNP significantly increased their ability to upregulate the wound tissue level of VEGF and EGF, the enhancement mechanism has not been documented to date, warranting further investigation.

Regarding non-diabetic acute wounds, the levels of VEGF and EGF in untreated wounds were 47 $\pm$ 4.24 pg mg^{-1} and 78 $\pm$ 4.24 pg mg^{-1}, respectively (figures 10(B) and (C). These values were significantly ($p \leqslant 0.05$) higher than their levels in the untreated diabetic wounds (22.5 $\pm$ 0.7 pg mg^{-1} and 31.5 $\pm$ 0.71 pg mg^{-1}, respectively), corroborating literature information [87]. Z-MS@scaffold treatment significantly ($p \leqslant 0.05$) increased VEGF and EGF levels to 90 $\pm$ 2.83 pg mg^{-1} and 139.5 $\pm$ 2.12 pg mg^{-1}, respectively. The pronounced upregulation of both growth factors by Z-MS@scaffold in acute wounds relative to chronic wounds attested the greater efficacy of the scaffold in treating acute wounds.

In summary, wound healing assessment at the macroscopic, microscopic and molecular levels provided evidence for the high efficacy of the DZ-MS@scaffold for treating challenging diabetic wounds and the aptness of the simpler Z-MS@scaffold formulation for accelerating effective healing of acute wounds. The current findings confirmed the versatility of the adopted 3D printing technique/rationale as a customization tool capable of addressing the demand for tailored wound healing bioactive materials.

4. Conclusion

We successfully developed a novel simple method for the fabrication of 3D printed NF hydrogel scaffolds for regenerative applications using 3D printing as the sole technique. The method involves endowing the hydrogel construct with an ECM-mimicking fibrous structure of multilevel porosity by dispersing injectable discrete polymer NF MS in the hydrogel ink rather than incorporating an electrospun nanofiber layer within the construct, as established to date. The method provides flexible customizability via 3D printing-associated tailoring of scaffold geometry and porosity as well as bioactive functionalization of MS

elements. *In vitro* characterization data and *in vivo* wound healing performance of Z-MS@scaffold and DZ-MS@scaffold provided evidence for versatile tailoring of scaffolds for regenerative healing of infected diabetic wounds as a model of chronic wounds and the less challenging non-diabetic acute wounds. Data ascertained for the first time the *in vivo* wound healing efficacy of DDAB-nano ZnO-activated scaffolds, provided that the nanomaterial is delivered by a carrier system such as polymeric NF MS. In fact, the carrier host did improve the nanomaterial dispersibility, physicochemical properties, antibacterial activity and wound healing performance, as demonstrated in the current study. Our findings provide insight into the opportune and promising convergence of structurally and chemically tailoring engineered constructs and 3D printing versatility for the fabrication of advanced customizable bioactive materials for diverse biomedical applications.

Data availability statement

All data that support the findings of this study are included within the article (and any supplementary files).

Acknowledgments

The authors gratefully acknowledge the valuable contribution of Dr Michael G Shehat, lecturer of microbiology, Department of Microbiology and Immunology, Faculty of Pharmacy, Alexandria University, Alexandria, Egypt to the conduction of the PCR study and the provision of primers.

Conflict of interest

The authors declare that there are no competing financial interests nor personal relationships that could have influenced the work reported in this paper.

Funding information

This work was supported by the Academic Thesis Research Fund (ATRF), Faculty of Pharmacy, Alexandria University (ATRF-420016).

ORCID iDs

Salma E El-Habashy https://orcid.org/0000-0003-3891-5049
Hoda M Eltaher https://orcid.org/0000-0001-5602-2696

References

[1] Wilkinson H N and Hardman M J 2020 Wound healing: cellular mechanisms and pathological outcomes *Open Biol.* **10** 200223
[2] Zhang Y, Chen W, Feng W, Fang W, Han X and Cheng C 2023 Multifunctional chondroitin sulfate based hydrogels for promoting infected diabetic wounds healing by chemo-photothermal antibacterial and cytokine modulation *Carbohydrate Polym.* **314** 120937
[3] Solanki D, Vinchhi P and Patel M M 2023 Design considerations, formulation approaches, and strategic advances of hydrogel dressings for chronic wound management *ACS Omega* **8** 8172–89
[4] Eltaher H M, Blokpoel Ferreras L A, Jalal A R and Dixon J E 2022 Direct contact-mediated non-viral gene therapy using thermo-sensitive hydrogel-coated dressings *Biomater. Adv.* **143** 213177
[5] Norahan M H, Pedroza-González S C, Sánchez-Salazar M G, Álvarez M M and de Santiago G T 2023 Structural and biological engineering of 3D hydrogels for wound healing *Bioact. Mater.* **24** 197–235
[6] Bastidas J G, Maurmann N, Oliveira L, Alcantara B, Pinheiro C V, Leipnitz G, Meyer F, Oliveira M, Rigon P and Pranke P 2023 Bilayer scaffold from PLGA/fibrin electrospun membrane and fibrin hydrogel layer supports wound healing *in vivo Biomed. Mater.* **18** 025020
[7] Yu H, Li Y, Pan Y, Wang H, Wang W, Ren X, Yuan H, Lv Z, Zuo Y and Liu Z 2023 Multifunctional porous poly (L-lactic acid) nanofiber membranes with enhanced anti-inflammation, angiogenesis and antibacterial properties for diabetic wound healing *J. Nanobiotechnol.* **21** 110
[8] Xiong Y, Chen L, Liu P, Yu T, Lin C, Yan C, Hu Y, Zhou W, Sun Y and Panayi A C 2022 All-in-one: multifunctional hydrogel accelerates oxidative diabetic wound healing through timed-release of exosome and fibroblast growth factor *Small* **18** 2104229
[9] Sharma A D, Jarman E H and Fox P M 2023 Scoping review of hydrogel therapies in the treatment of diabetic chronic wounds *Plastic Reconstr. Surg. Glob. Open* **11** e4984
[10] Freedman B R, Hwang C, Talbot S, Hibler B, Matoori S and Mooney D J 2023 Breakthrough treatments for accelerated wound healing *Sci. Adv.* **9** eade7007
[11] Markakis K, Faris A R, Sharaf H, Faris B, Rees S and Bowling F L 2018 Local antibiotic delivery systems: current and future applications for diabetic foot infections *Int. J. Low Extrem. Wounds* **17** 14–21
[12] Abdel-Rahman L M, Eltaher H M, Abdelraouf K, Bahey-El-Din M, Ismail C, Kenawy E-R S and El-Khordagui L K 2020 Vancomycin-functionalized Eudragit-based nanofibers: tunable drug release and wound healing efficacy *J. Drug Deliv. Sci. Technol.* **58** 101812
[13] Turzańska K, Adesanya O, Rajagopal A, Pryce M T and Fitzgerald Hughes D 2023 Improving the management and treatment of diabetic foot infection: challenges and research opportunities *Int. J. Mol. Sci.* **24** 3913
[14] Miraj S S, Kurian S J, Rodrigues G S, Saravu K, Rao M, Raychaudhuri S P, Downs B W and Bagchi D 2023 Phytotherapy in diabetic foot ulcers: a promising strategy for effective wound healing *J. Am. Nutrition Assoc.* **42** 295–310
[15] El-Aassar M R, El-Beheri N G, Agwa M M, Eltaher H M, Alseqely M, Sadik W S and El-Khordagui L 2021 Antibiotic-free combinational hyaluronic acid blend nanofibers for wound healing enhancement *Int. J. Biol. Macromol.* **167** 1552–63
[16] Jiang H, Xu Q, Wang X, Shi L, Yang X, Sun J and Mei X 2023 Preparation of antibacterial, arginine-modified Ag nanoclusters in the hydrogel used for promoting diabetic infected wound healing *ACS Omega* **8** 12653–63
[17] Wang L, Hussain Z, Zheng P, Zhang Y, Cao Y, Gao T, Zhang Z, Zhang Y and Pei R 2023 A mace-like heterostructural enriched injectable hydrogel composite for on-demand promotion of diabetic wound healing *J. Mater. Chem.* B **11** 2166–83
[18] Zhang J, Liu H, Che T, Zheng Y, Nan X and Wu Z 2023 Nanomaterials for diabetic wound healing: visualization and bibliometric analysis from 2011 to 2021 *Front. Endocrinol.* **14** 1124027

[19] Vijayakumar V, Samal S K, Mohanty S and Nayak S K 2019 Recent advancements in biopolymer and metal nanoparticle-based materials in diabetic wound healing management *Int. J. Biol. Macromol.* **122** 137–48
[20] Pino P, Bosco F, Mollea C and Onida B 2023 Antimicrobial nano-zinc oxide biocomposites for wound healing applications: a review *Pharmaceutics* **15** 970
[21] Loera-Valencia R, Neira R E, Urbina B P, Camacho A and Galindo R B 2022 Evaluation of the therapeutic efficacy of dressings with ZnO nanoparticles in the treatment of diabetic foot ulcers *Biomed. Pharmacother.* **155** 113708
[22] Metwally W M, El-Habashy S E, El-Nikhely N A, Mahmoud H E, Eltaher H M and El-Khordagui L 2023 Nano zinc oxide-functionalized nanofibrous microspheres: a bioactive hybrid platform with antimicrobial, regenerative and hemostatic activities *Int. J. Pharm.* **638** 122920
[23] Hadisi Z, Farokhi M, Bakhsheshi-Rad H R, Jahanshahi M, Hasanpour S, Pagan E, Dolatshahi-Pirouz A, Zhang Y S, Kundu S C and Akbari M 2020 Hyaluronic acid (HA)-based silk fibroin/zinc oxide core–shell electrospun dressing for burn wound management *Macromol. Biosci.* **20** 1900328
[24] Uchida D T and Bruschi M L 2023 3D printing as a technological strategy for the personalized treatment of wound healing *AAPS PharmSciTech* **24** 41
[25] Farsheed A C, Thomas A J, Pogostin B H and Hartgerink J D 2023 3D printing of self-assembling nanofibrous multidomain peptide hydrogels *Adv. Mater.* **35** 2210378
[26] Kong F, Mehwish N and Lee B H 2023 Emerging albumin hydrogels as personalized biomaterials *Acta Biomater.* **157** 67–90
[27] Jiao T, Lian Q, Lian W, Wang Y, Li D, Reis R L and Oliveira J M 2023 Properties of collagen/sodium alginate hydrogels for bioprinting of skin models *J. Bionic Eng.* **20** 105–18
[28] Song Z, Wang J, Tan S, Gao J and Wang L 2023 Conductive biomimetic bilayer fibrous scaffold for skin regeneration *Colloids Surf.* A **656** 130211
[29] He H and Molnár K 2021 Fabrication of 3D printed nanocomposites with electrospun nanofiber interleaves *Addit. Manuf.* **46** 102030
[30] Liu C, Wang Z, Wei X, Chen B and Luo Y 2021 3D printed hydrogel/PCL core/shell fiber scaffolds with NIR-triggered drug release for cancer therapy and wound healing *Acta Biomater.* **131** 314–25
[31] Akkineni A R, Spangenberg J, Geissler M, Reichelt S, Buechner H, Lode A and Gelinsky M 2021 Controlled and local delivery of antibiotics by 3D core/shell printed hydrogel scaffolds to treat soft tissue infections *Pharmaceutics* **13** 2151
[32] Wang W, Liu M, Shafiq M, Li H, Hashim R, El-Newehy M, El-Hamshary H, Morsi Y and Mo X 2023 Synthesis of oxidized sodium alginate and its electrospun bio-hybrids with zinc oxide nanoparticles to promote wound healing *Int. J. Biol. Macromol.* **232** 123480
[33] Lin Y, Xu J, Dong Y, Wang Y, Yu C, Li Y, Zhang C, Chen Q, Chen S and Peng Q 2023 Drug-free and non-crosslinked chitosan/hyaluronic acid hybrid hydrogel for synergistic healing of infected diabetic wounds *Carbohydrate Polym.* **314** 120962
[34] Viswanathan K, Kim I, Kasi G, Sadeghi K, Thanakkasaranee S and Seo J 2020 Facile approach to enhance the antibacterial activity of ZnO nanoparticles *Adv. Appl. Ceram.* **119** 414–22
[35] Guadarrama Bello D, Fouillen A, Badia A and Nanci A 2020 Nanoporosity stimulates cell spreading and focal adhesion formation in cells with mutated paxillin *ACS Appl. Mater. Interfaces* **12** 14924–32
[36] Nour E M, El-Habashy S E, Shehat M G, Essawy M M, El-Moslemany R M and Khalafallah N M 2023 Atorvastatin liposomes in a 3D-printed polymer film: a repurposing approach for local treatment of oral candidiasis *Drug Deliv. Transl. Res.* (https://doi.org/10.1007/s13346-023-01353-4)
[37] Maiz-Fernández S, Barroso N, Pérez-Álvarez L, Silván U, Vilas-Vilela J L and Lanceros-Mendez S 2021 3D printable self-healing hyaluronic acid/chitosan polycomplex hydrogels with drug release capability *Int. J. Biol. Macromol.* **188** 820–32
[38] Weinstein M P, Limbago B, Patel J, Mathers A, Burnham C and T M 2018 *CLSI standard M07-Methods for Dilution Antimicrobial Susceptibility Tests for Bacteria that Grow Aerobically* 11th edn (Clinical and Laboratory Standards Institute) p 112p
[39] Derossi A, Caporizzi R, Azzollini D and Severini C 2018 Application of 3D printing for customized food. A case on the development of a fruit-based snack for children *J. Food Eng.* **220** 65–75
[40] El-Habashy S E, El-Kamel A H, Essawy M M, Abdelfattah E-Z A and Eltaher H M 2021 3D printed bioinspired scaffolds integrating doxycycline nanoparticles: customizable implants for *in vivo* osteoregeneration *Int. J. Pharm.* **607** 121002
[41] Noh I, Kim N, Tran H N, Lee J and Lee C 2019 3D printable hyaluronic acid-based hydrogel for its potential application as a bioink in tissue engineering *Biomater. Res.* **23** 3
[42] Khalid A, Madni A, Raza B, Islam M U, Hassan A, Ahmad F, Ali H, Khan T and Wahid F 2022 Multiwalled carbon nanotubes functionalized bacterial cellulose as an efficient healing material for diabetic wounds *Int. J. Biol. Macromol.* **203** 256–67
[43] Cam M E, Ertas B, Alenezi H, Hazar-Yavuz A N, Cesur S, Ozcan G S, Ekentok C, Guler E, Katsakouli C and Demirbas Z 2021 Accelerated diabetic wound healing by topical application of combination oral antidiabetic agents-loaded nanofibrous scaffolds: an *in vitro* and *in vivo* evaluation study *Mater. Sci. Eng.* C **119** 111586
[44] Li Q, Gong S, Yao W, Yang Z, Wang R, Yu Z and Wei M 2021 Exosome loaded genipin crosslinked hydrogel facilitates full thickness cutaneous wound healing in rat animal model *Drug Deliv.* **28** 884–93
[45] Tan W S, Arulselvan P, Ng S-F, Mat Taib C N, Sarian M N and Fakurazi S 2019 Improvement of diabetic wound healing by topical application of Vicenin-2 hydrocolloid film on Sprague Dawley rats *BMC Complement Altern. Med.* **19** 1–16
[46] Shafei S, Khanmohammadi M, Heidari R, Ghanbari H, Taghdiri Nooshabadi V, Farzamfar S, Akbariqomi M, Sanikhani N S, Absalan M and Tavoosidana G 2020 Exosome loaded alginate hydrogel promotes tissue regeneration in full-thickness skin wounds: an *in vivo* study *J. Biomed. Mater. Res.* A **108** 545–56
[47] Ding Y-W, Zhang X-W, Mi C-H, Qi X-Y, Zhou J and Wei D-X 2023 Recent advances in hyaluronic acid-based hydrogels for 3D bioprinting in tissue engineering applications *Smart Mater. Med.* **4** 59–68
[48] Taghizadeh M *et al* 2022 Chitosan-based inks for 3D printing and bioprinting *Green Chem.* **24** 62–101
[49] Vieira de Souza T, Malmonge S M and Santos A R Jr 2021 Development of a chitosan and hyaluronic acid hydrogel with potential for bioprinting utilization: a preliminary study *J. Biomater. Appl.* **36** 358–71
[50] Sadeghianmaryan A, Naghieh S, Alizadeh Sardroud H, Yazdanpanah Z, Afzal Soltani Y, Sernaglia J and Chen X 2020 Extrusion-based printing of chitosan scaffolds and their *in vitro* characterization for cartilage tissue engineering *Int. J. Biol. Macromol.* **164** 3179–92
[51] Daly A C, Critchley S E, Rencsok E M and Kelly D J 2016 A comparison of different bioinks for 3D bioprinting of fibrocartilage and hyaline cartilage *Biofabrication* **8** 045002
[52] Hernández-Sosa A, Ramírez-Jiménez R A, Rojo L, Boulmedais F, Aguilar M R, Criado-Gonzalez M and Hernández R 2022 Optimization of the rheological properties of self-assembled tripeptide/alginate/cellulose hydrogels for 3D printing *Polymers* **14** 2229
[53] Cleetus C M, Alvarez Primo F, Fregoso G, Lalitha Raveendran N, Noveron J C, Spencer C T, Ramana C V and Joddar B 2020 Alginate hydrogels with embedded ZnO nanoparticles for wound healing therapy *Int. J. Nanomed.* **15** 5097–111

[54] Lavigne J-P, Hosny M, Dunyach-Remy C, Boutet-Dubois A, Schuldiner S, Cellier N, Yahiaoui-Martinez A, Molle V, La Scola B and Marchandin H 2021 Long-term intrahost evolution of Staphylococcus aureus among diabetic patients with foot infections *Front. Microbiol.* **12** 741406
[55] Yan D, Li Y, Liu Y, Li N, Zhang X and Yan C 2021 Antimicrobial properties of chitosan and chitosan derivatives in the treatment of enteric infections *Molecules* **26** 7136
[56] Romanò C, Vecchi E D, Bortolin M, Morelli I and Drago L 2017 Hyaluronic acid and its composites as a local antimicrobial/antiadhesive barrier *J. Bone Joint Infection* **2** 63–72
[57] Said S S, Aloufy A K, El-Halfawy O M, Boraei N A and El-Khordagui L K 2011 Antimicrobial PLGA ultrafine fibers: interaction with wound bacteria *Eur. J. Pharm. Biopharm.* **79** 108–18
[58] Pasquet J, Chevalier Y, Pelletier J, Couval E, Bouvier D and Bolzinger M-A 2014 The contribution of zinc ions to the antimicrobial activity of zinc oxide. Colloids and Surfaces A *Physicochem. Eng. Asp.* **457** 263–74
[59] Sthoer A, Hladílková J, Lund M and Tyrode E 2019 Molecular insight into carboxylic acid-alkali metal cations interactions: reversed affinities and ion-pair formation revealed by non-linear optics and simulations *Phys. Chem. Chem. Phys.* **21** 11329–44
[60] Burger K, Illés J, Gyurcsik B, Gazdag M, Forrai E, Dékány I and Mihályfi K 2001 Metal ion coordination of macromolecular bioligands: formation of zinc(II) complex of hyaluronic acid *Carbohydrate Res.* **332** 197–207
[61] Mahmood U, Masood R, Afzal M A, Raza Z A, Abid S, Zahir A, Hussain T and Nazir A 2022 Development of zinc, silver, and hyaluronic acid mediated wet spun alginate fibers for potential wound care applications *J. Ind. Text.* **51** 1916S–30S
[62] Chen W, Xu Y, Liu Y, Wang Z, Li Y, Jiang G, Mo X and Zhou G 2019 Three-dimensional printed electrospun fiber-based scaffold for cartilage regeneration *Mater. Des.* **179** 107886
[63] Liu Q, Li Q, Xu S, Zheng Q and Cao X 2018 Preparation and properties of 3D printed alginate–chitosan polyion complex hydrogels for tissue engineering *Polymers* **10** 664
[64] Galarraga J H, Kwon M Y and Burdick J A 2019 3D bioprinting via an in situ crosslinking technique towards engineering cartilage tissue *Sci. Rep.* **9** 19987
[65] El-Habashy S E, El-Kamel A H, Essawy M M, Abdelfattah E-Z A and Eltaher H M 2021 Engineering 3D-printed core–shell hydrogel scaffolds reinforced with hybrid hydroxyapatite/polycaprolactone nanoparticles for *in vivo* bone regeneration *Biomater. Sci.* **9** 4019–39
[66] Majhy B, Priyadarshini P and Sen A K 2021 Effect of surface energy and roughness on cell adhesion and growth—facile surface modification for enhanced cell culture *RSC Adv.* **11** 15467–76
[67] Ilhan E *et al* 2020 Development of Satureja cuneifolia-loaded sodium alginate/polyethylene glycol scaffolds produced by 3D-printing technology as a diabetic wound dressing material *Int. J. Biol. Macromol.* **161** 1040–54
[68] Hudak R, Trebunova M, Zivcak J and Kottfer D 2018 Scaffolds for tissue engineering—introduction *Acta Tecnol.* **4** 67–70
[69] Glover K, Mathew E, Pitzanti G, Magee E and Lamprou D A 2022 3D bioprinted scaffolds for diabetic wound-healing applications *Drug Deliv. Transl. Res.* **13** 2096–109
[70] Zhao H X, Li L H, Ding S, Liu C X and Ai J Y 2018 Effect of porous structure and pore size on mechanical strength of 3D-printed comby scaffolds *Mater. Lett.* **223** 21–24
[71] Pan W, Qi X, Xiang Y, You S, Cai E, Gao T, Tong X, Hu R, Shen J and Deng H 2022 Facile formation of injectable quaternized chitosan/tannic acid hydrogels with antibacterial and ROS scavenging capabilities for diabetic wound healing *Int. J. Biol. Macromol.* **195** 190–7
[72] Davachi S M, Haramshahi S M A, Akhavirad S A, Bahrami N, Hassanzadeh S, Ezzatpour S, Hassanzadeh N, Malekzadeh Kebria M, Khanmohammadi M and Bagher Z 2022 Development of chitosan/hyaluronic acid hydrogel scaffolds via enzymatic reaction for cartilage tissue engineering *Mater. Today Commun.* **30** 103230
[73] Wang Y, Chen Y, Zheng J, Liu L and Zhang Q 2022 Three-dimensional printing self-healing dynamic/photocrosslinking gelatin-hyaluronic acid double-network hydrogel for tissue engineering *ACS Omega* **7** 12076–88
[74] Mania S, Ryl J, Jinn J-R, Wang Y-J, Michałowska A and Tylingo R 2019 The production possibility of the antimicrobial filaments by co-extrusion of the PLA pellet with chitosan powder for FDM 3D printing technology *Polymers* **11** 1893
[75] Meng X, Lu Y, Gao Y, Cheng S, Tian F, Xiao Y and Li F 2021 Chitosan/alginate/hyaluronic acid polyelectrolyte composite sponges crosslinked with genipin for wound dressing application *Int. J. Biol. Macromol.* **182** 512–23
[76] Nath S D, Abueva C, Kim B and Lee B T 2015 Chitosan–hyaluronic acid polyelectrolyte complex scaffold crosslinked with genipin for immobilization and controlled release of BMP-2 *Carbohydrate Polym.* **115** 160–9
[77] Tottoli E M, Dorati R, Genta I, Chiesa E, Pisani S and Conti B 2020 Skin wound healing process and new emerging technologies for skin wound care and regeneration *Pharmaceutics* **12** 735
[78] Raziyeva K, Kim Y, Zharkinbekov Z, Kassymbek K, Jimi S and Saparov A 2021 Immunology of acute and chronic wound healing *Biomolecules* **11** 700
[79] Sultan S and Mathew A P 2018 3D printed scaffolds with gradient porosity based on a cellulose nanocrystal hydrogel *Nanoscale* **10** 4421–31
[80] Nor Azlan A Y H, Katas H, Mh Busra M F, Salleh N A M and Smandri A 2021 Metal nanoparticles and biomaterials: the multipronged approach for potential diabetic wound therapy *Nanotechnol. Rev.* **10** 653–70
[81] Liao W, Duan X, Xie F, Zheng D, Yang P, Wang X and Hu Z 2023 3D-bioprinted double-crosslinked angiogenic alginate/chondroitin sulfate patch for diabetic wound healing *Int. J. Biol. Macromol.* **236** 123952
[82] Bai H, Kyu-Cheol N, Wang Z, Cui Y, Liu H, Liu H, Feng Y, Zhao Y, Lin Q and Li Z 2020 Regulation of inflammatory microenvironment using a self-healing hydrogel loaded with BM-MSCs for advanced wound healing in rat diabetic foot ulcers *J. Tissue Eng.* **11** 2041731420947242
[83] Vaid R, Yildirim E, Pasquinelli M A and King M W 2021 Hydrolytic degradation of polylactic acid fibers as a function of pH and exposure time *Molecules* **26** 7554
[84] Xu F, Zhang C and Graves D T 2013 Abnormal cell responses and role of TNF-α in impaired diabetic wound healing *Biomed Res. Int.* **2013** 754802
[85] Berlanga-Acosta J, Camacho-Rodríguez H, Mendoza-Marí Y, Falcón-Cama V, García-Ojalvo A, Herrera-Martínez L and Guillén-Nieto G 2022 Epidermal growth factor in healing diabetic foot ulcers: from gene expression to tissue healing and systemic biomarker circulation *MEDICC Rev.* **22** 24–31
[86] Le V A T, Trinh T X, Chien P N, Giang N N, Zhang X-R, Nam S-Y and Heo C-Y 2022 Evaluation of the performance of a ZnO-nanoparticle-coated hydrocolloid patch in wound healing *Polymers* **14** 919
[87] Patel S, Srivastava S, Singh M R and Singh D 2019 Mechanistic insight into diabetic wounds: pathogenesis, molecular targets and treatment strategies to pace wound healing *Biomed. Pharmacother.* **112** 108615
[88] Heim J, Felder E, Tahir M N, Kaltbeitzel A, Heinrich U R, Brochhausen C, Mailänder V, Tremel W and Brieger J 2015 Genotoxic effects of zinc oxide nanoparticles *Nanoscale* **7** 8931–8